Title
Shockwave Spectroscopy of Nanoparticles

Author
Merkle, Maxwell Graham

Publication Date
2011

Peer reviewed|Thesis/dissertation

Shockwave Spectroscopy of Nanoparticles

By

Maxwell Graham Merkle

A dissertation submitted in partial satisfaction of the
requirements for the degree of

Doctor of Philosophy in Chemistry

in the
GRADUATE DIVISION
of the
UNIVERSITY OF CALIFORNIA, BERKELEY

Committee in Charge:
Professor A. Paul Alivisatos
Professor Stephen R. Leone
Professor Roger W. Falcone

Shockwave Spectroscopy of Nanoparticles

By

Maxwell Graham Merkle

Doctor of Philosophy in Chemistry

University of California, Berkeley

Professor A. Paul Alivisatos, Chair.

This dissertation examines the effects of laser-generated shockwaves on colloidally prepared nanocrystals. Their microscopic structure is first examined utilizing gold nanoparticles. The properties under scrutiny in the first study are used to then initiate a polymorphic phase transition in CdSe quantum dots. In the final study, hollow CdS particles are used to show the utility of nanoparticles as possible energy attenuation materials.

In gold nanoparticles it is shown, for the first time, a direct observation of the effect of density increase on the optical properties of gold nanoparticles. The splitting of the plasmon resonance into two distinct peaks illustrates the result of a uniaxial compression characteristic of a shock wave.

The behavior of CdSe nanocrystals shocked to stresses of 2–3.75 GPa has been studied. Above 3 GPa a near-complete disappearance of the first excitonic feature and broadening of the low-energy absorption edge were observed, consistent with a wurtzite to rocksalt structural transformation. The transformation pressure is reduced relative to hydrostatic compression in a diamond anvil cell. Also, the rate of the phase transition increases. These effects are attributed to shock induced shear stress along the reaction coordinate. The especially rapid rate observed for a 3.75 GPa shock suggests multiple nucleation events per particle.

Hollow CdS nanospheres have been fractured under the action of laser-induced shock waves. Transmission electron microscopy (TEM) and scanning electron microscopy (SEM) have been used to image the recovered fragmented particles. Additionally, time-resolved measurements of the transmission of the shock wave through a polymer layer containing hollow nanospheres have been carried out. The hollow nanospheres can attenuate the transmitted shock above a threshold stress. At the highest shock stresses measured, the shock attenuation layer acts as a composite shocked above its elastic limit.

To these ends we show that nanoparticles are useful in studying and altering the properties of shockwaves. Shockwaves are also shown to be useful in high time-resolution studies of the morphological processes in solids, using nanocrystals as the archetypical, single-domain sample.

Acknowledgements

Professor Paul Alivisatos has been an extraordinary mentor, whose brave guidance-through-freedom has given me the opportunity to explore, falter, and learn from my mistakes in research. I know this has helped shape the kind of scientist that I will become.

Dr. Joshua Wittenberg was the best mentor I could never have thought to ask for. He guided me through all of the practical aspects of the experiments we developed together, and was an amicable partner in research and a great person to look to for academic and professional guidance.

And though I only single out Josh for his help and guidance through my studies, there was no real shortage of friendly, helpful people in the group, who provided help without hesitation. It is in this sort of community that science can truly thrive.

My parents, Mark and Peggy, have been unbelievably supportive. They are amazing people, and loving parents, who gave me everything (and more than) I needed.

My new fiancée and partner in life, Stephanie Felo, has been an inspiration to me. I truly believe that there is nothing she cannot do. I do not have a truer friend in this world, and consider myself extremely lucky to have found her.

Despite the trying times I have experienced throughout my graduate career, it is not without a great deal of nostalgia that I will look back upon these times in my life. This is because I have had better friends, family, mentors, and co-workers than I could have ever imagined.

For my friends and family

Table of Contents

Chapter 1:
Introduction

Shockwaves provide a way to rapidly pressurize a sample. They are able to bring the sample to a state that is prepared at very high density, pressure, and temperature. By utilizing them in an experimental context, it becomes possible to initiate thermochemical reactions and phase transitions on demand [1,2].

Typically, experiments of this nature are carried out at large government laboratories and involve shock-initiating events such as expolosive charges, gas driven projectiles or high-energy laser pulses. The low experimental repetition-rate and high cost per shock can either lead to noisy data or limit studies to recovery experiments.

Thermochemical processes can be probed by ultrafast optical spectroscopies. Ultrafast phenomena are normally studied by high rep. rate, short pulse (~ fs-ps) spectroscopic techniques. Techniques such as time-resolved fluorescence and transient absorption spectroscopies are routinely used to investigate photochemical processes such as electron-transfer in materials. Even complex nonlinear spectroscopies such as femtosecond stimulated raman spectroscopy and four wave mixing techniques have become much more common in recent years.

The strength of these techniques relies on the photophysical preparation of a large fraction of a population of interest within the probed region of a sample by using a short, large flux optical pump pulse. This prepared state can then go on to excite molecular dynamics that can be studied by appropriately chosen, time-resolved spectroscopic techniques. Sufficient signal to noise ratios can be obtained by averaging over more events at a given time delay between the pump and the probe pulses. The time resolution of these techniques is also partly dependent on how quickly the state that is being studied can be prepared. It also depends upon how short the pump and probe pulses are.

It has recently been demonstrated that the moderate energy pulses (~ 1mJ) available from a commercially available, table-top laser apparatus can produce and study phenomena associated with shockwaves. Some of these studies, termed “nano-shock” techniques, include probing the molecular dynamics of polymers behind a shock front [3], the desorption dynamics of self-assembled monolayers [4], and the initiation of shock-sensitive explosives [5].

Experiments of this type represent a distinctly different way of performing pump-probe spectroscopic studies. In these studies, the sample is *directly prepared* in a non-equilibrium mechanical state, leading to the direct excitation of thermochemical processes, rather than them being actuated as a result of the system decaying from a photophysically prepared state. The pump is mechanical, and the same spectroscopies can be done by the probe pulses of choice, leading to a unique way to study materials in extreme conditions. The shockwaves travel on the order of tens of nanometers per picosecond through a molecular material such as a polymer. This finite transit time, along with the intrinsic rise-time of the shockwave in the material is what determines the time resolution of these shockwave spectroscopic techniques. This means that as long as the probe pulse is short enough (less than the shock transit time through the sample) and the sample can be made thin enough (while not sacrificing too much signal), the dynamics of these materials can be studied directly.

Mechanical disturbances such as plastic deformations and phase transitions propagate through a material at a finite speed that is approximately the speed of sound of that material. For

example, in heavier inorganic materials (like gold and the cadmium chalcogenides) is two to five times faster than the speed of sound of molecular crystals and polymeric solids. A shockwave traveling through a nanocrystal/polymer composite imposes a stress through compression of the polymer that is seen by the analyte crystals as roughly constant across their charictaristic length scales (1-10 nm). In order to study processes that occur behind the shock front, we employ slightly larger particles (such as the 20 nm gold particles in Chapter 2) that more effectively sense the anisotropy of the shockwave's compression.

The goal of this dissertation is to provide several examples of how shockwaves and nanoparticles interact with one another, and how each is uniquely suited to answer scientific questions about the other.

1.1 Shockwaves

Shockwaves are pervasive, if not ubiquitous phenomena that we experience in one way or another nearly daily [1,2]. They are evident in the crack of gunfire, the boom from an overhead supersonic aircraft, or in the pile-up of a traffic jam. They all represent situations in which the material flow (or shock velocity) is faster than the natural speed of sound of the system. A simple way to envision the way they are created in a solid is to picture the case where a driver projectile or piston is incident upon a material. For lower incident driver speeds, the disturbance propagates elastically as a traveling wave through the material.

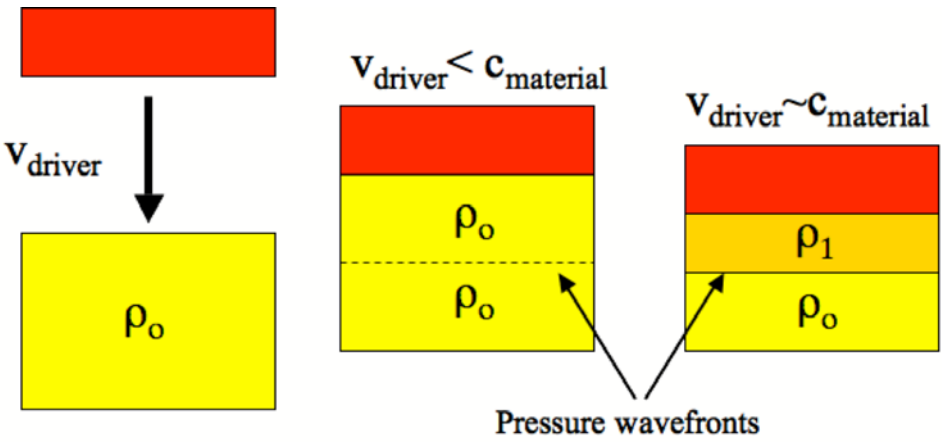

Figure 1.1: Schematic representation of an archetypical driver (or piston) with a velocity, v, upon a material of an ambient density r_o, and speed of sound, c.

In materials, shockwaves are created by a driving pulse incident upon it with a speed that is some large fraction of the materials longitudinal sound velocity. The shock has discontinuous changes in material properties across the shock front. Enforcing the conservation of energy and mass across the disturbance yields the very general Rankine-Hugoniot (or more commonly, simply "Hugoniot") equations:

$$P_1 - P_0 = \frac{U_S U_P}{V_0}$$

$$1 - \frac{V_1}{V_0} = \frac{U_P}{U_S}$$

$$E_1 - E_0 = \frac{1}{2}(P_1 - P_0)(V_0 - V_1)$$

where the subscript "1" indicates a property of the material behind the shock front, and subscript "0" indicates the unshocked material. P is the pressure, V is the specific volume ($1/\rho$) where ρ is the bulk density, and E is the internal energy per unit mass. U_S is the velocity of the shock front with respect to the laboratory coordinates, and U_P is the particle velocity (or equivalently, driver velocity). It is useful to depict these parameters graphically in a Rankine-Hugoniot PV curve (RH curve). This is one of the pairs of thermodynamic variables that may be plotted against one another in what is often termed, simply, a "Hugoniot" for a material.[6] The Hugoniot relations are often used as equations of state for shock processes once enough data is compiled for a material, though the state of a shocked material cannot be calculated analytically given a set of initial conditions.

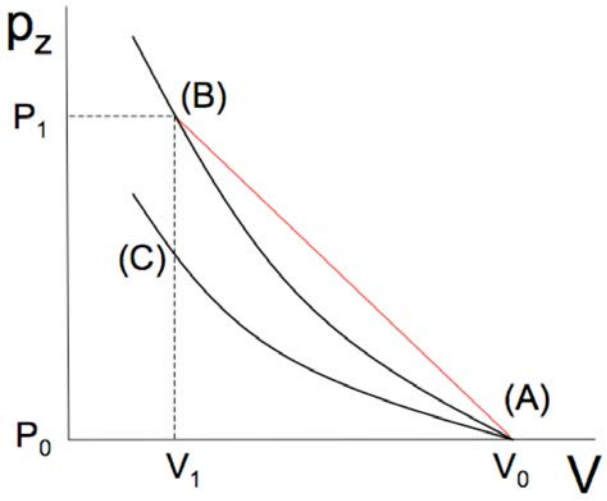

Figure 1.2: Depiction of an isentrope (lower solid curve), Hugoniot (upper solid curve), and Rayleigh line (red line) in the PV plane.

Although RH-relations relate thermodynamic variables across a shockwave to one another, there is an important distinction between them and a thermodynamic equation of state to keep in mind. That is that while every point on an isentrope (for example) represents a continuum of equilibrium states, every point on a Hugoniot curve represents a final shocked state. These neighboring states are not accesable from other shocked states, but instead from an initial, ambient state. The point B on the above Hugoniot is connected to point A by a Rayleigh line, the slope of which characterizes the shock front's velocity. Due to the irreversible nature of the process, a series of experiments must be performed, each of which yields a Rayleigh line connecting the initial and shocked states. The collection of data from those experiments can be plotted as a Hugoniot.

While instantaneous compression has no theoretical restrictions, since the conservation of mass, momentum, and energy are accounted for by the RH-relations. Rarefaction, however, cannot occur instantaneously, as it would violate the second law of thermodynamics. In general, the process of relaxation is complex and material dependent.

Microscopically, compression occurs inertially along the direction of shock propagation. The initial uniaxial compression yields to shear and volume relaxation behind the front, the

details of which are dermined by the intermolecular or inter-atomic interactions of the media through which the disturbance propagates [2,3].

1.2 Thermodynamic and Mechanical Properties of Nanocrystals

The mechanical, thermodynamic, and kinetic properties of nanocrystals vary with respect to their bulk material counterparts. This partially results from the energetic contributions from the surface of the crystallite. The total energy of a system varies as *N*, the number of particles, while the surface energy goes like $N^{2/3}$. This implies that as *N* gets smaller, the properties of the atoms on the surface make a greater contribution to the total energy and other properties of the material.

Generally, the surface tension is neglected in the calculation for the free energy of a material, since the surface comprises a miniscule fraction of the total volume. However, as the surface to volume ratio increases, the surface tension cannot be neglected as it may represent a significant portion of the free energy. One result of the stronger influence of the surface tension in nanocrystals is that the melting temperature [7,11] of a nanocrystal is lower than that of the bulk material by an amount [12]:

$$T_B - T_N = \frac{2T_N}{L\rho_S R_S}\left[\gamma_S - \gamma_L\left(\frac{\rho_S}{\rho_L}\right)\right]$$

where T_B and T_N are the respective melting temperatures of the bulk and of a particle of radius R. L is the latent heat of fusion per mole, ρ is the density and γ is the surface tension. For a 3 nm CdS spherical nanocrystal, that difference is 800 ^{o}C.

The polymorphic wurtzite-rocksalt structural phase transformation that occurs in bulk CdSe and CdS occurs at a much higher pressure in nanocrystals. This is related to both the thermodynamic and kinetic details of the transition process.

Small semiconductor nanocrystals can be thought of as defect-free single crystalline domains since defects are easily annealed from the small crystals during the nanocrystal growth process. The wurtzite-rocksalt phase transformation in CdSe and CdS is believed to occur via a martensitic-type mechanism. Such a transformation is characterized by the concerted motion of atoms in the crystal, with most of the bonds remaining intact. In a discrete nanocrystal, this transformation must be accompanied by a shape-change. Changing the shape can expose different crystalline facets. In general, since the crystals are synthesized at high temperatures, the facets that are exposed by such a transition are usually higher in energy. The result is a greater free energy change upon undergoing the phase transformation for nanocrystals than for bulk materials and, hence, a higher thermodynamic phase transition pressure. The increase in thermodynamic phase transition pressure with decreasing size is a significant effect that has been studied previously [13].

Additionally, and representing an even greater fraction of the transition pressure discrepancy between finite size and bulk, is the large kinetic barrier that must be surmounted in order to effect the transformation in nanocrystals. This leads to a broad hysteresis between the forward and reverse transformations. The kinetic barrier is the result of inelastic bond rearrangements at the surface of the nanocrystal upon transformation. Though the thermodynamic phase transition pressure may be elevated relative to that of the bulk by <1 to a few GPa, depending on the size of the nanocrystal, the increase in the observed transition pressure attributed to the kinetic barrier may be as much as 4-5 GPa. Overall, the effect of the surface is much stronger in nanomaterials than in their bulk counterparts.

As discussed in Chapter 4, the nanoscopic sizes of these crystals lead to a simplification of

transformation dynamics, allowing one to study the dynamics of the actual transition more directly. By producing shockwaves one can initiate and study phase transitions on the timescales over which they occur.

While ultrafast x-ray diffraction experiments are still in their infancy with respect to their corresponding equilibrium measurement techniques, optical spectroscopies are readily available to probe the electronic structure of materials of interest under shock compression. This can provide an indirect way to probe the structure of a material. Nanocrystals' optical spectra display unique features that are charactaristic of both their constituant material properties (such as morphology) and intrinsic to their nanoscopic length scales (such as size and shape).

1.3 Electronic Structure and Spectroscopy of Nanocrystals

In semiconductor nanocrystals the UV-vis extinction spectrum is dominated by sub-band-gap resonances. The transitions these resonances represent are subject, not only to the periodic boundary conditions of the lattice (band properties) but also to the additional potential barrier introduced by the existence of the surface of the particle. The surfaces have profound effects on the onset of these electronic transitions and can be loosely interpreted by considering the problem as a particle in a box, with a potential that is infinite outside of the particle. The energy level spacing of such a system is given by:

$$E_n = \frac{\hbar^2 \pi^2 n^2}{2mR^2}$$

For small R (particle diameter) and n is the principle quantum number of the pseudo-excitonic state of the electron-hole pair. The metric for gauging whether a particle is in the strong (small R) or weak (large R) confinement regime, is the exciton Bohr radius, a_B. This number represents the average, ground-state distance between the electron and hole in a bulk solid. As R approaches the size of the Bohr radius, dielectric confinement effects dominate the electron-hole interaction, the levels increase in separation, and the electron and hole wavefunctions take the form of the spherical harmonics [14]. Near these values of R, the band gap,[*] and the resulting optical properties (absorption edge, fluorescence, etc.) can be modulated by changing the size of the particle.

Though small, the particles still contain a sizeable number of unit-cells (~100-1000). Thus the behavior of the bands and their corresponding response from the extended solids is still instructive for interpreting spectra. Energy bands in extended solids are the eigenvalues of each of the symmetry-adapted linear combination of atomic orbitals. There are many atoms in a solid, so the set of eigenstates around a constituant basis state appear to form a continuum with their corresponding energies differing much less than k_BT [15,16].

The electronic structure of a material is, in general, modulated by strain. Pressure induces spectral changes, mixing of electronic states, in solids, molecules [17] and in nanoparticles [18,19].

The electronic bands (and thus the density of states) tend to spread in energy when a material is compressed as the orbital overlap between unit-cells increases. The s bands are the most sensitive, followed by the p, and so on. Roughly speaking, the more spherically symmetric bands are the most sensitive to strain in the lattice [19,20]. This is of particular interest to those

[*] This is not strictly correct, in this case, as the above equation describes the first hydrogen-like transition, not the ionization energy of an electron at the top of the valence band.

interested in building electronic networks of structures that are grown epitaxially, since particles grown on a surface have a built-in strain due to lattice mismatches.

In metals, the electrons in the conduction band can couple resonantly to an incident electric field through surface plasmon oscillations. The energy at which these electrons couple most strongly to the external field is called the surface plasmon resonance (SPR). In many metal particles, these bands are well isolated from the core levels of the atoms in the lattice (Al, Na, etc.) and the behaviour of the resonance is well-described by a free electron (Drude) model. All of these plasma resonances are in the ultraviolet spectral region. In closed d-shell metals (Cu, Ag, Au), the d-bands are close in energy to the electronic states, which have an atomic basis that is mostly of an s charicter, that cross the Fermi surface. Thus, the electronic excitations between d and sp-like states couple strongly with the excitation of conduction electrons. [21-23].

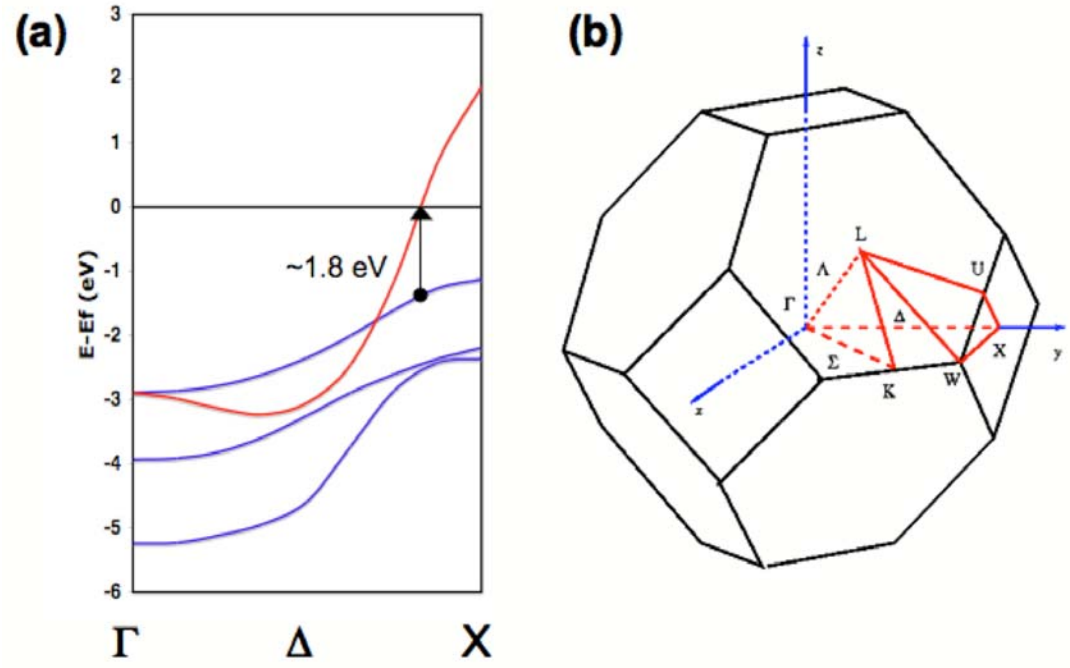

Figure 1.4: (a) The band-structure of gold along high symmetry points in the first Brillouin zone shown in (b), the onset of allowed interband transitions is shown. (c) The extinction spectrum for colloidal solution of 20 nm spheres with the onset of interband transitions (*) near the high-symmetry point X is shown. (part a is adapted from ref. 24)

There have been few studies of how the plasmon energy shifts with pressure because of the small observed change over the stresses examined. This is due to the necessity of using a fluid to transmit the stress to an ensemble of particles. Since the ω_{SPR} depends strongly on the refractive index of the medium ($\omega_{SPR}=2\varepsilon_{media}$) for small, spherical particles, the observed spectral changes are dominated by a shift in the resonance to lower energies. This is mostly due to the compressibility of the surrounding media [25]. In a polymer-nanocrystal composite, such as the ones examined herein, the bulk compressibility is much less, and the resulting change in refractive index is negligible [26].

Discussed hereafter are the interactions of shockwaves with nanoparticles. The effect of the shock's transient anisotropic stress upon gold particles is explored. Shocks of a moderate strength (~2 GPa) are shown to be sufficient to induce topological changes in gold nanoparticles that are born out in the transient absorption spectra.

It is shown that it is possible to use these highly anisotropic stress states behind the shock front to induce a structural transition in an ensemble of CdSe nanoparticles below the transition pressure observed in hydrostatic experiments.

Nanoparticles are then shown to be able to attenuate the amount of stress transmitted through a sample. Upon loading beyond a critical stress (1.5 GPa) ceramic, hollow CdS spherical shells fracture, dissipating energy.

The first of the experiments shows that Au nanocrystals can be used to probe the microscopic nature of the shockwave. Then using that very microscopic, transient we initiate a polymorphic transition in CdSe nanoparticles far below the critical stress for transition under hydrostatic conditions. And finally, we show that it is also possible to alter the properties of a shockwave with nanostructured CdS particles.

Chapter 2:

Experimental Methods

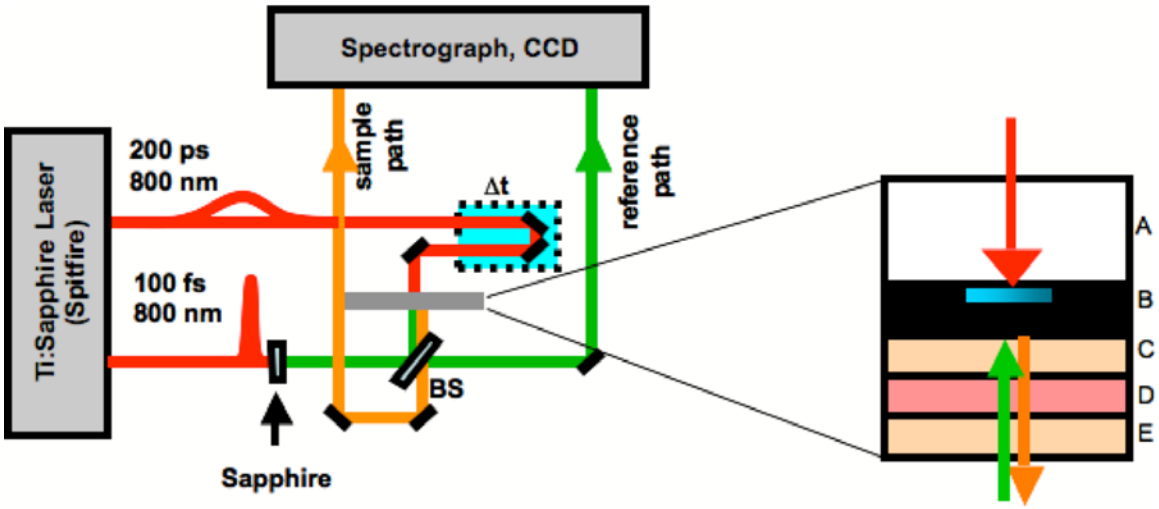

Figure 2.1: Schematic of (left) Experimental apparatus and (right) target array cross section showing: A. Glass wafer, B. Vapor-coated aluminum with "shock front" (in blue), C. PVB buffer layer, D. Polymer/sample layer containing Au, CdSe, R-640, or polymer only, E. Thick epoxy overlayer.

Shockwaves are generated in these experiments by laser ablation using a near-IR laser pulse incident upon a thin metal layer upstream from the sample of interest. Our regeneratively amplified Ti:sapphire laser system (Spitfire, Spectra-Physics) produces 1 mJ pulses with a central wavelength of 800 nm. The repetition rate was set to 250 Hz for this experiment. The output was split within the amplifier system. The shock generation pulse remained uncompressed following amplification (900 μJ, 200 ps, FWHM), and the probe pulse was compressed (100 fs, FWHM) and focused on a 1 mm thick sapphire crystal to generate broadband white light continuum. The bandwidth was adjusted using a variable slit in the subsequent prism chirp compensator. The shock pulse travelled along an optical delay path and was then focused to a 250 μm diameter spot on the rear of the target [Fig. 2.2(a)]. A half-wave plate and polarizer prior to the delay line were used for continuous variable attenuation of the shock pulse.

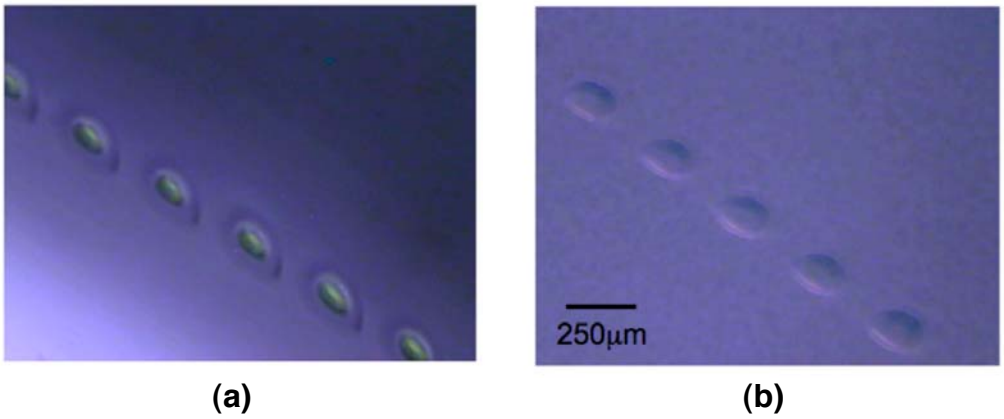

Figure 2.2: Optical microscope image of partially ablated Al layer (a) pump side (rear) (b) probe side (front).

Since the aluminum shock-generation layer was damaged by the pulse, the target was mounted on a translation stage in order to expose a fresh area for each shock. Fig. 2.2 depicts a typical row of shocked spots that are well-spaced and uniform, with a thin layer of Al remaining for probe reflection from the front surface. The dimpling of the surface is less pronounced in the fully assembled targets. The broadband continuum pulse (~100 fs, FWHM) was focused to an 80 μm spot and reflected from the aluminum layer in a collinear double-pass geometry. A portion of the continuum pulse bypassed the sample and was used as a reference for the absorption measurement. Sample and reference beams were dispersed by a spectrograph onto a charge-coupled device (CCD).

Data were software-averaged, with the absorption spectrum at each time delay consisting of an entire row of ~100 shocked spots. A background correction was performed on each spectrum by subtracting the absorption of a blank target, i.e. one with the same multilayer structure, under the same shock conditions, but without R-640 or nanocrystals of interest (Au spheres, CdSe spheres, or CdS shells) added to the sample layer. To avoid errors due to spectral differences between rows of spots on a target, optical density changes (ΔOD/OD) were calculated by subtracting the peak OD value from the spectrum of a shocked row from that of the spectrum of the same row un-shocked and dividing by the initial peak intensity to get ΔOD/OD.

The samples for shockwave spectroscopy were prepared in a monolithic layered format (Figure 2.1, right). The sample starts with a rigid substrate (Corning^{TM} 0211 glass wafers, 200 μm thick), so that the focus of the incident laser pulses and their subsequent optical paths do not change. These are vapor coated with 1.5 μm of aluminum (Cascade Optical Corp.). A 1 μm thick (±5%) polyvinyl(butyral-co-vinyl alcohol-co-vinyl acetate) (PVB, Aldrich) buffer layer was spin-coated from chloroform solution on each target. The purpose of the buffer layer is that it allows the shock front time to steepen prior to reaching the sample. If the buffer layer is too thick, however, (>6 μm) a significant portion of the shock energy will have dissipated prior to reaching the sample. Buffer layers were cured at ~120 ^{o}C for 30 minutes to cross-link the polymer chains, reducing their solubility in chloroform to prevent dissolution of the buffer layer during sample layer application. Next, a 250 nm (±10%) sample layer, containing either 8 wt.% rhodamine-640 perchlorate dye (R-640, Exciton) in PVB as a pressure probe or a nanocrystal (CdSe, or CdS)/polymer sample of choice is deposited by spin-coating. The process is different in the case of Au nanoparticles, in that the sample is deposited electrostatically, using polyelectrolyte layer deposition [33]. The details of this method are discussed in Chapter 3.

It is important to ensure that the layers comprising the target structure are impedance-matched, in order to allow transmission of the shock pressure at the interface between layers. Shock reflection can cause attenuation of the pressure reaching downfield layers and, depending on the specific target, shock ring-up whereby the sample layer is not compressed in a single compression cycle, but a series of compressions as the shock reverberates through the target. The resulting shock is not instantaneous, but can be approximated as an isentropic compression. The shock impedance, *Z*, of a material is given by:

$$Z = \rho_o U_s$$

For weak shocks in which the shock velocity and longitudinal sound velocity, c_0, are similar, this can be approximated by:

$$Z = \rho_o c_o$$

The pressure transmitted when a shock traverses the interface between two layers of different material is given by:

$$P_{tr} = \frac{2P_o}{1 + \frac{Z_a}{Z_b}}$$

This applies in the case where $Z_a > Z_b$ and reduces the transmitted stress for every layer-pair besides the case where they are comprised of the same material. Polymeric materials with similar shock impedances were used for each layer of the target structure.

In order to measure the pressure at a given time delay, a pressure sensitive dye is used. The pressure calibrant is prepared in a way analogous to the nano-crystalline containing sample, such that the samples are mechanically equivalent over the pressure ranges studied. The most advantageous dye for our spectral range is Rhodamine-640 (R-640). In addition to exhibiting a transition in the visible with a large absorption cross-section, the dye is soluble in the same range of solvents as the nanocrystalline analytes of interest. The dye's absorption maximum shifts to a lower energy with pressure.

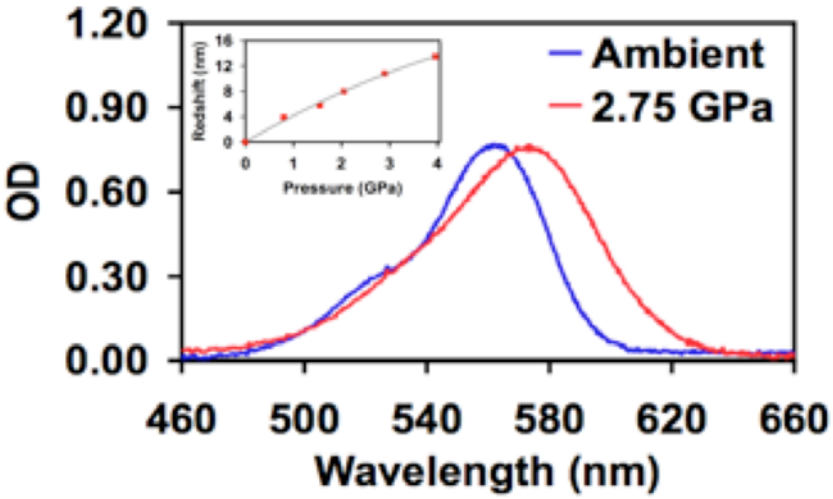

Figure 2.3: UV-visible absorption spectrum of R-640 dye shocked in our apparatus to a pressure of 2.75GPa. Inset: Shift of R-640 absorption feature vs. applied hydrostatic pressure in a DAC.[29]

The red-shift of the Rhodamine-640 absorption peak [Fig. 2.3] with increasing pressure has been well-characterized [29] in polymer films and is seen to be independent of temperature. The width of the peak is the only feature of the spectrum that varies with any measureable amount with changes in temperature.

The duration of the optical shock-driving pump pulse does not directly determine the time resolution of the experiment. The transit time convoluted with intrinsic rise-time (the viscoelastic response of the polymer material behind the front spreads out the rise-time) determines the time resolution of the experiment. In general, thinner sample layers yield finer time resolutions. It is roughly equal to the thickness of the sample layer divided by the velocity of the shockwave (5 nm/ps in the polymer lalyers discussed above).

The shock driving optical pulse affects the pressure transients, which we need to be able to characterize. These transients depend predictably on the incident pulse energy (typically, higher energies yield higher peak pressures). With all else being equal, it is possible to vary the peak shock pressure by simply varying the average pump power. We accomplish this by changing the angle of the quarter waveplate with respect to the orientation of a polarizer.

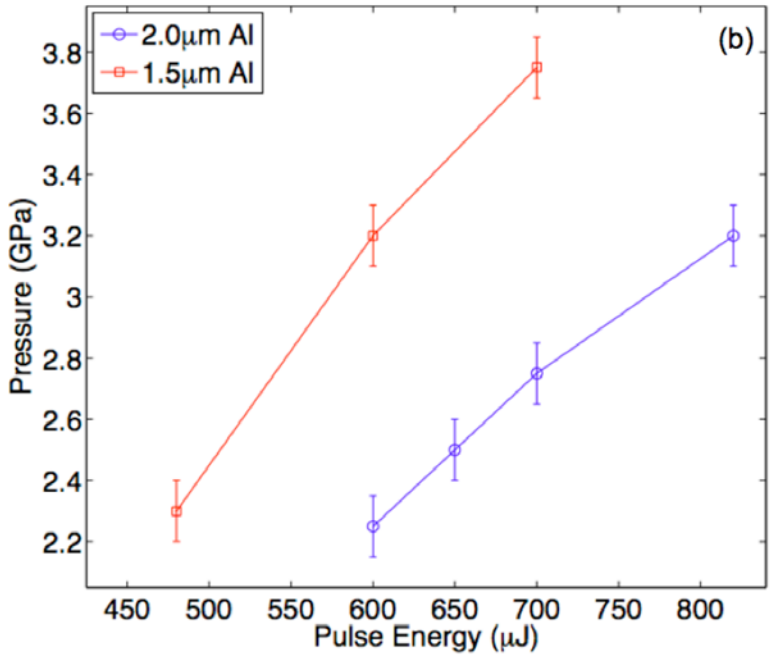

Figure 2.4 : Peak pressure achieved vs. pulse energy for Al ablation films of different thicknesses (1.5 μm (red) and 2.0 μm Al)

Higher peak pressures are observed at higher pulse energies. We can only measure a maximum pressure around 3.7 GPa produced from a 1.5 μm thick film. At higher energies than 700 μJ the target region is totally destroyed and there is no material left to reflect the probe pulses. Lower pressures are produced from the 2.0 μm thick film than the 1.5 μm thick film at the same incident pulse energy. This is because in the thicker film, the shockwave must traverse a larger amount of remaining Al to enter the polymer layers, giving it more time to interact with the dense aluminum and dissipate. Higher peak pressures should be achievable in the thicker film, but we were limited by the amount of energy our laser could produce per pulse (~1 mJ).

The pressure transients depend in a much more complex way on the other parameters in our laser apparatus. In order to demonstrate the repeatability of the technique, the pressure transients were recorded over the course of two days (Figure 2.5).

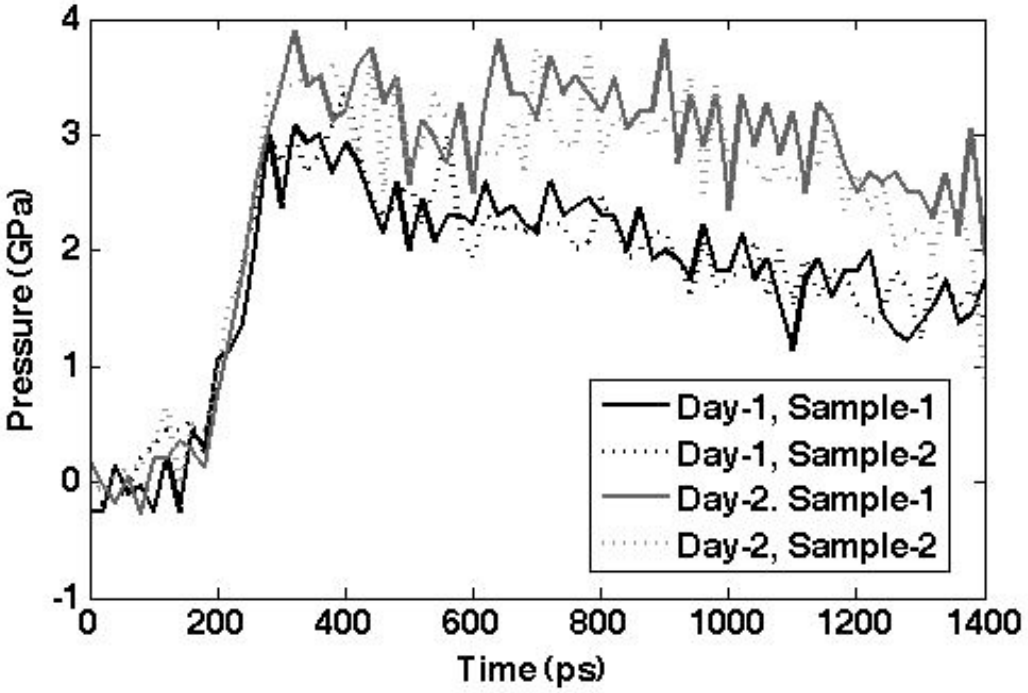

Figure 2.5: Pressure transients taken from separate samples over two days.

On the first day, two separate pressure calibrations were preformed on separate, but identically fabricated sample substrates. The experimental apparatus was then fully shut down and was turned on and re-optimized on the second day. The transients taken on the same day are, for all intents and purposes, identical. However, the differences that manifest themselves over the course of shut-down/restart of the apparatus are those that could be explained by considering the details of the ablation-driving pulse. Pulse duration has been shown to affect shock strength [27]. Also, of note is the fact that there is probably some hardening that occurs in the sample layers over long periods of time. To avoid these types of discrepancies, all experiments described herein are performed in the same day (per experiment), using samples that are all produced simultaneously.

2.2 Molecular Dynamics Simulations for Au Nanoparticles

To reveal the microscopic details of the structural response of a gold nanocrystal pressurized by a shock wave, we simulate spherical gold nanocrystals with a diameter of 6 nm under uniaxial stress. The nanocrystals are spheres cut out of a bulk FCC gold lattice. For gold, we use the glue potential by Ercolessi et al. [30], which accurately reproduces many structural properties of the bulk material and has also been successfully applied in studies of gold nanoparticles [31]. A single particle is placed in a simulation box that is elongated in the direction of the applied stress, with dimensions of 12x9x9 nm; periodic boundary conditions are used. The equations of motion are integrated with the velocity Verlet algorithm [32] with a time step of 1 fs. In a quick annealing run of 50 ps, the temperature of the crystal is lowered from 800 K to the experimental temperature of T = 300 K by velocity rescaling.

Then, the crystal is surrounded by a pressure medium of repulsive particles of the WCA type [33]. In particular, we choose the following parameters, designed to reproduce the compressibility of bulk PMMA: $\varepsilon = 0.2$ eV, $\sigma = 0.3$ nm, and $m = 32$ amu. The same potential is used for interactions of WCA particles with gold atoms. We use the following scheme to insert the particles into the simulation box: The particles are placed on an FCC lattice with nearest neighbor distance $d = 1.3\,\sigma$. To remove particles that overlap with gold atoms, we calculate for every particle its potential energy E with all gold atoms. We keep only particles with low E. In particular, we remove a particle from the simulation with probability $1 - \exp(-E/k_BT)$, where k_B is the Boltzmann constant. Next, we run the dynamics at constant volume, keeping the temperature at $T = 300$ K. The WCA crystal melts and forms a dense liquid. After 15 ps, we introduce harmonic bonds (spring constant $k = 200$ eV/nm^2) between close-by WCA particles, turning the liquid into an amorphous soild. We use an algorithm that produces a random network of particles where (almost) every particle is bound to 5 neighbor particles. The resulting solid has a bulk modulus that closely matches the bulk modulus of PMMA at pressures between 0 and 1.2 GPa [34].

After another equilibration period of 15 ps, we start simulating under conditions of constant stress using the approach of Parrinello and Rahman [35]. For 300 ps, we increase the externally applied stress in the x-direction by 0.15 GPa every 5 ps, leaving all other components of the stress tensor at zero.

Chapter 3:

The Shock-Compression of Au Nanoparticles

3.1 Introduction:

Shockwaves, among other things, are a tool that allows one to quickly access high pressure states in a material. Their short rise-times in polymeric materials (~100 ps) and composites thereof, allow rapid pressurization of an immersed sample. As discussed in Chapter 1, this gives one the opportunity to perform pump-probe spectroscopy in a situation where the pump is a purely mechanical process, the shockwave. This is in contrast to more traditional pump-probe techniques that use an optical pump to excite a sample into a dissociative state to initiate a structural effect. As in an all-optical technique, the time resolution is, in part, limited by the width of the driving pulse. This is true in shock-spectroscopy, with the additional caveat that it is not just the width of the driving pulse, but its width in comparison to the time that the disturbance takes to traverse the analyte as it is being probed. The ideal sample is thus one that can be made very thin, while still giving a good signal to noise ratio. Au nanoparticles satisfy this in that they can be deposited in a monolayer and intimately sandwiched in between polymer supports. Their high extinction coefficient allows monolayer samples to be prepared without worrying about mottling their spectral response with interparticle effects. Even at the low loading fractions (3% by area), we are able to observe peak extinction optical densities ~ 0.25.

In addition to their short rise-times, shockwaves have a complex structure. Following an initial uniaxial compression phase (during the rise of the stress transient), the sample undergoes microscopic relaxation events characteristic of both volume and shear relaxation events. These events have been studied theoretically [1], and experimentally by considering the processes that could contribute to rise-time broadening across mechanically different samples [3]. While processes observed behind shock fronts are often explained in this context, there are few, if any direct measurements of these different processes by an imbedded analyte.

Gold pillars have been shown to deform at relatively low stresses (~1 GPa) [36] relative to what can be achieved in ablation-induced shockwaves in polymeric materials (~4 GPa) [29]. The mechanism of this deformation is a sliding of {111} planes allowing piston displacement [30].

Here, it is shown that the initial uniaxial nature of the shockwave of a moderate strength can deform 20 nm Au nanocrystals imbedded in a polymer matrix. Upon yielding, the crystallites deform into oblate spheroidal shapes. This shape change is monitored by observing the shifting and splitting of the surface plasmon resonance (SPR) of the particles into short and long axis modes, giving a direct probe of the shock's initial anisotropy.

3.2 Experimental Methods:

3.2.1 Sample Architecture:

Shock targets (Fig. 4.2(b)) were assembled from 1 inch diameter, 200 μm thick, Corning™ 0211 glass wafers, vapor coated with 1.5 μm of aluminum (Cascade Optical Corp.). A 1 μm thick (±5%) polyvinyl(butyral-co-vinylalcohol-co-vinyl acetate) (PVB, Aldrich) buffer layer was spin-coated from chloroform solution on each target. The purpose of the buffer layer is to allow the shock front time to steepen prior to reaching the sample. If the buffer layer is too thick, however, (>6 μm) a significant portion of the shock energy will have dissipated prior to reaching the sample [37]. Buffer layers were cured at 120 ^{0}C for 30 minutes to cross-link the polymer chains and drive off the remaining chloroform.

The next series of layers was applied using a method developed by Decher and colleagues [38,39]. The cured, dried substrates were immersed in a solution of polyethyleneimine (MW = 50 kDa, Aldrich). After 20 minutes, they were removed, rinsed in deionized water, and dried under a stream of nitrogen. The substrates were then placed in a solution of 3 mM sodium polystyrene sulfonate (168 kDa) and 1M NaCl (Aldrich). The wafers were recovered after 20 minutes and were then rinsed in deionized water and immersed in a soluion that also contained 1M NaCl and 3 mM polyallylamine hydrochloride. The substrates were recovered and rinsed again after 20 minutes had passed. They were then dried under a stream of nitrogen and the dipping process was repeated in the PSS and PAH solutions for three more cycles. The polymer-functionalized substrates were then immersed in a gold sol containing 20 nm Au nanoparticles in a citrate solution (Brittish Biocel Inc.). After 3 hours, the substrates were removed, rinsed, and treated a final time with the PAH solution.

For targets containing Rhodamine-640, the targets were spin-coated with an 8 wt.% Rhodamine 640 Perchlorate dye (R-640, Exciton) and PVB dissolved in chloroform. An over-layer of 5-minute epoxy (Devcon™) was applied, and flattened with a layer of cover glass to remove air pockets and protect the entire multi-layer structure. Layer thicknesses were determined using a KLA-Tencor Alpha-Step IQ profilometer. Thickness error was determined by measuring many areas of each layer.

3.2.2 Spectroscopic Methods

The arrangement of the optical table and data collection techniques are described in Chapter 2.

3.2.3 Molecular Dynamics Simulations

The methods for these simulations are discusses in Chapter 2.

3.3 Results

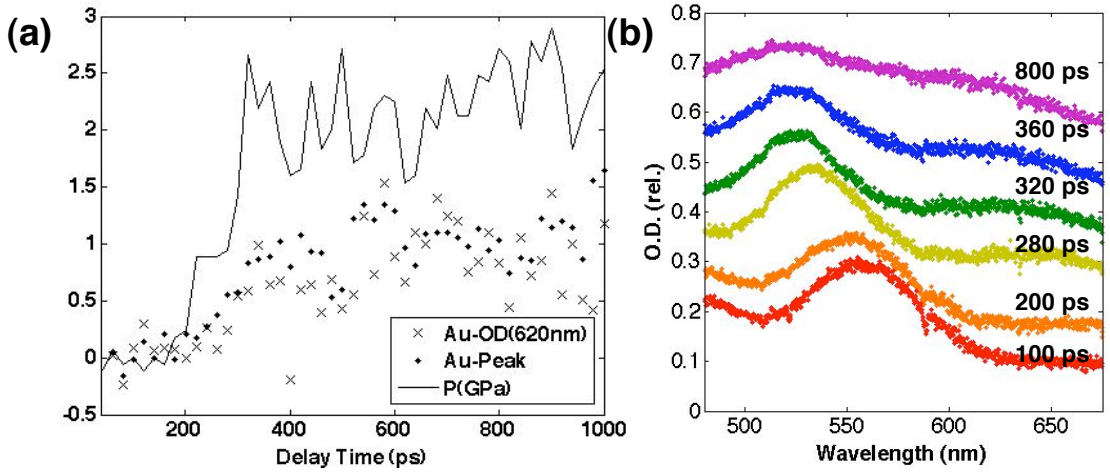

Figure 3.1: (A) Shockwave-induced transients. The solid line traces the pressure at each delay time. The black dots track the relative position of the original SPR peak and the crosses show the rise of a new peak at lower energies. The pressure is given in GPa (marked on the abcissa), while the values of the peak wavelength and OD of the Au SPR modes are in arbitrary units. (B) Broadband extinction spectra of Au nanoparticles at different delay times (spectra are offset vertically for clarity).

3.3.1 Effects on the Extinction Spectra, The Density Change:

The compression of a sample of gold nanoparticles can have several possible effects upon the electronic structure, and the overall extinction of the sample. By compressing a discrete particle, it is possible to increase the density of conduction electrons, simply by changing the size of the particle (thereby increasing the density). The electron density, n, is well known to be related to the bulk plasma frequency, as follows:

$$\omega_{SPR} \sim \omega_P = \left(\frac{ne^2}{m\varepsilon_O} \right)^{1/2}$$

Here, ω_{SPR} and ω_P are the SPR and bulk plasma frequencies, respectively, and m is the effective mass of the electrons in the conduction band. As the electron density increases, so should the plasmon resonance frequency. By taking the number of electrons in the conduction band to be constant, one can arrive at a relative volume for any blue-shifted frequency. This is plotted below.

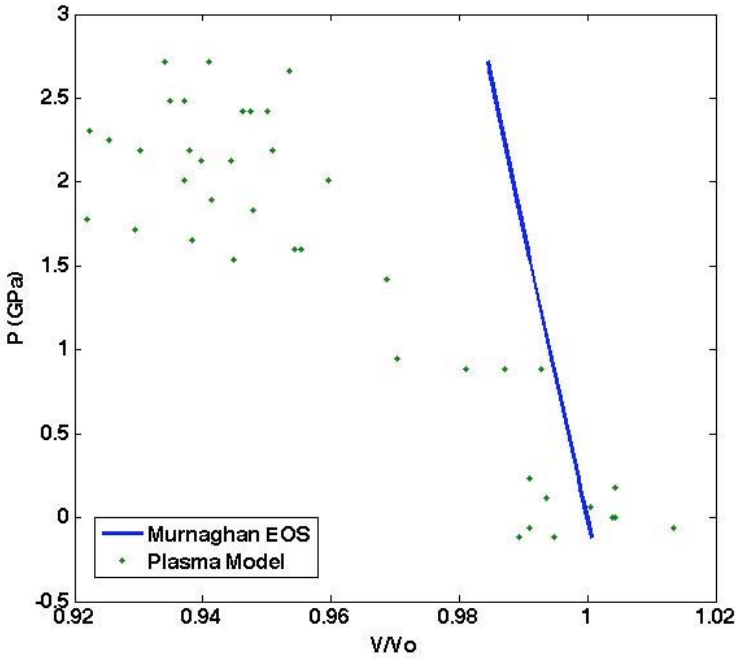

Figure 3.2: Experimentally derived relative volumes at different pressures arrived at using the plasma model are plotted in green, using the shock data. Also plotted in blue is the Murnaghan equation of state for gold over the same region of pressure.

The model shows very little agreement with the well-established Murnaghan equation of state. It is difficult to believe that gold could be compressed by the ~8% predicted by the plasma model without massive changes to the electronic structure [40,26].

The energy bands do not stay constant with the imposed strain. There is also much reason to believe that they broaden unevenly, given that the states that contribute to the interband transitions near the Fermi energy are of s (conduction band) and d character (valence band) [26]. This leads to an increased energy difference at any given point on the reciprocal lattice near the Fermi level. The Fermi level does not necessarily stay constant, and should shift to higher energies as strain increases, as it also increases with increased number-density of electrons.

Both of these effects, working, in concert, would produce a higher energy for the onset of interband transitions. As discussed previously, these transitions strongly couple to the SPR. There little reason to doubt that changing the onset of these transitions to higher energy would not have the same effect upon the SPR. The position of the SPR depends, in detail, upon the high pressure band structure of gold. The calculations have not been done for strain-augmented lattices, so it is difficult to make a quantitative estimate of the contribution of these factors to the SPR.

3.3.2 Shape Effects

One can certainly imagine a deformable sphere with a uniaxial force exerted upon it deforming in a manner commensurate with the geometry of the applied force. That is to say, that it should be deformed in a manner consistent with the material's Poisson ratio (0.44 in Au), or in a similar, though more microscopically complex manner in the presence of slip-dislocations. Both buckling and the sliding of {111} planes has been observed experimentally [40] and

modeled previously [41] in nanopillars at stresses lower than measured in the current work (P < 1 GPa). In isolated, spherical particles this deformation would result in a particle with an oblate spheroidal shape.

For an isotropic distribution of oblate ellipsoidal metallic particles in a dielectric medium, the total extinction cross section <*C*> can be written as a sum of the absorption absorption (C_{abs}) and scattering (C_{scat}) cross sections:

$$\langle C \rangle = \langle C_{abs} \rangle + \langle C_{scat} \rangle = k\,\mathrm{Im}\left\{\frac{2}{3}\alpha_{long} + \frac{1}{3}\alpha_{short}\right\} + k^4 \Big/ 6\pi\left[\frac{2}{3}\left|\alpha_{long}\right|^2 + \frac{1}{3}\left|\alpha_{short}\right|^2\right]$$

$$\alpha_i = V\frac{\tilde{\varepsilon} - \varepsilon_m}{\varepsilon_m + L_i\left(\tilde{\varepsilon} - \varepsilon_m\right)}$$

Where the cross sections depend on the real and imaginary portions of the polarizability along an axis, i. For an ellipsoidal metallic particle the polarizability along the long and short axes are dependent upon the geometric factors L_i. These are arrived at analytically, by solving Laplace's Equation for the system of interest in the electrostatic approximation yielding:

$$L_{long} = \frac{g(e)}{2}\left[\frac{\pi}{2} - \tan^{-1} g(e)\right] - \frac{g^2(e)}{2}$$

Where:

$$g(e) = \left(\frac{1-e^2}{e^2}\right)^{1/2}$$

The factor g(e) is a function of the spheroid's eccentricity, e, which is the inverse of the aspect ratio. Having different polarizabilities along different axes splits the resonance in the visible region of the extinction spectra for anisotropic spheroids. The other geometric factors are given by $L_{short} = 1 - 2L_{long}$.

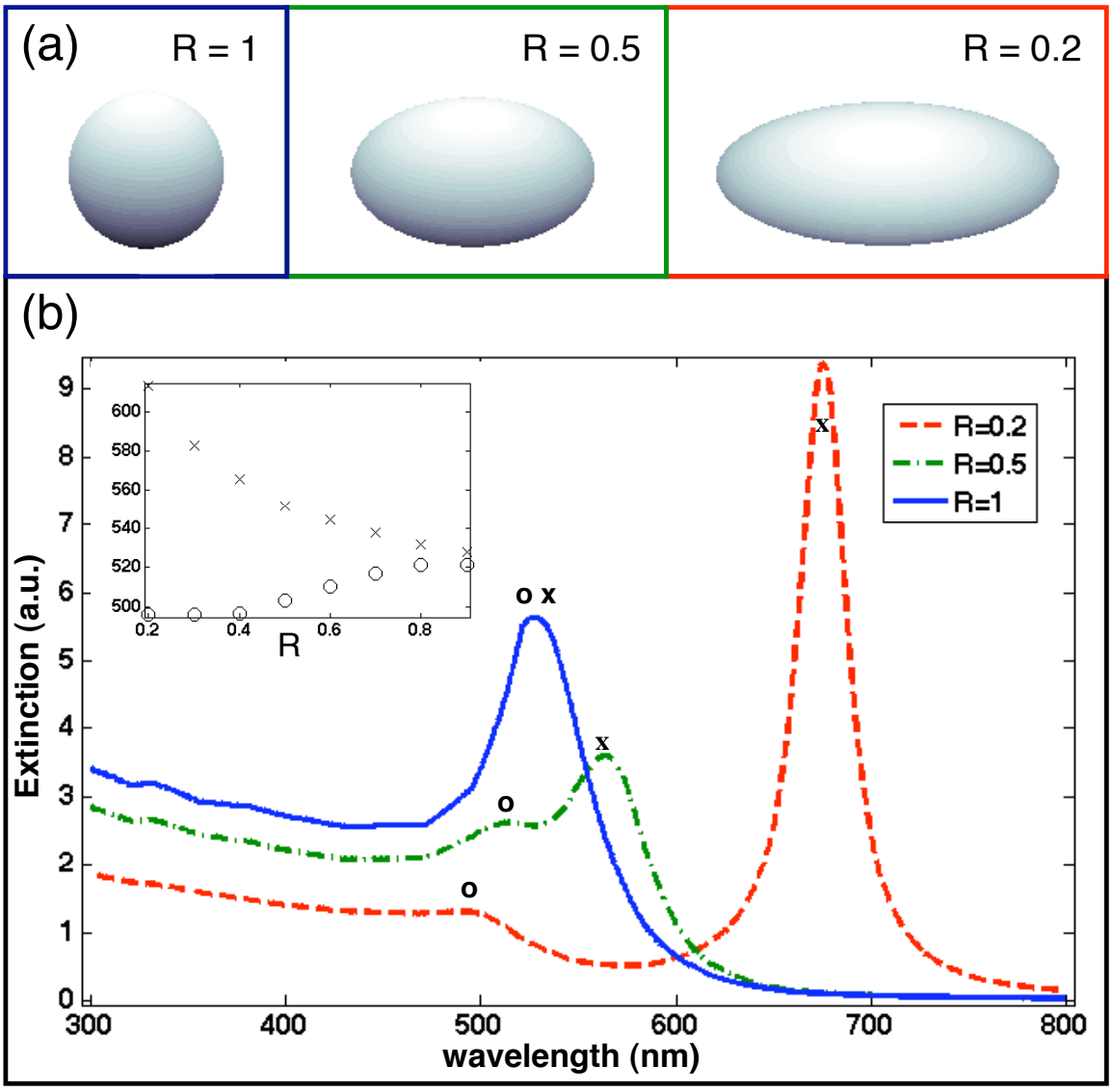

Figure 3.3: (A) Oblate spheroids with decreasing aspect ratio, R. (B) Calculated extinction spectra of isotropically oriented samples of spheroids for different aspect ratios. The inset shows the peak wavelength of the resonances corresponding to the short-axis (marked as "o") and long-axis (marked as "x") plasmon modes.

As the aspect ratio decreases, the peak that appears at lower energies is associated with the excitation of electrons along the longer axes. This peak corresponds to a more polarizable mode and is thus more intense than the short-axis mode.

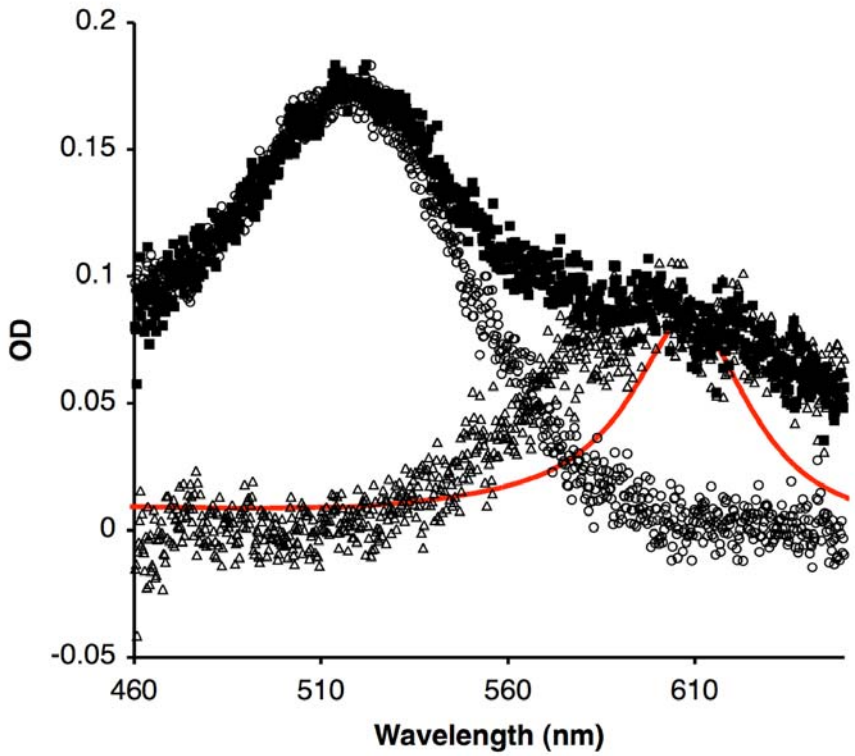

Figure 3.4: Extinction spectrum of gold nanoparticle sample (solid squares) at 360 ps (~2GPa). Ambient spectrum from an identical series of spots on the sample, shifted to higher energy. Difference spectrum (triangles) between the aforementioned spectra showing the appearance of the long-axis mode. Calculated long-axis mode (red line) of an R = 0.3 spheroid.

This shows that the spectrum can be decomposed into a shifted part that is unaffected by anisotropy, and a new resonance that is due to particles that are deformed. The additional width compared to the electrostatic calculations is, in part, due to sample shape inhomogeneities resulting from the sample size distribution. The peak's value depends exponentially on the length of the minor axes and is therefore extremely sensitive to variations in sizes and shapes [41]. This can be interpreted as follows: all of the particles experience the hydrodynamic strain associated with the compression wave (resulting in the shift of the primary resonance to higher energies), and some of the population is deformed (resulting in the appearance of a new, broad resonance at lower energy).

3.3.3 Molecular Dynamics Simulations

We preformed molecular dynamics calculations to further develop a picture of the microscopic, time-resolved behavior of the particles under a uniaxial compression wave. The details of the technique used to perform the simulations was discussed in detail in Chapter 2. In these simulations, a polymer mechanically and optically identical to polymethylmethacrylate is used as the pressure-transmitting medium as it is very well characterized. As seen in Figure 3.5, the compression of the nanocrystal occurs in the expected direction (coincident with that of the incident pressure wave). The crystallites modeled deform elastically, and then they undergo slip relaxation. This produces an irreverseable shape-change that is preserved upon decompression.

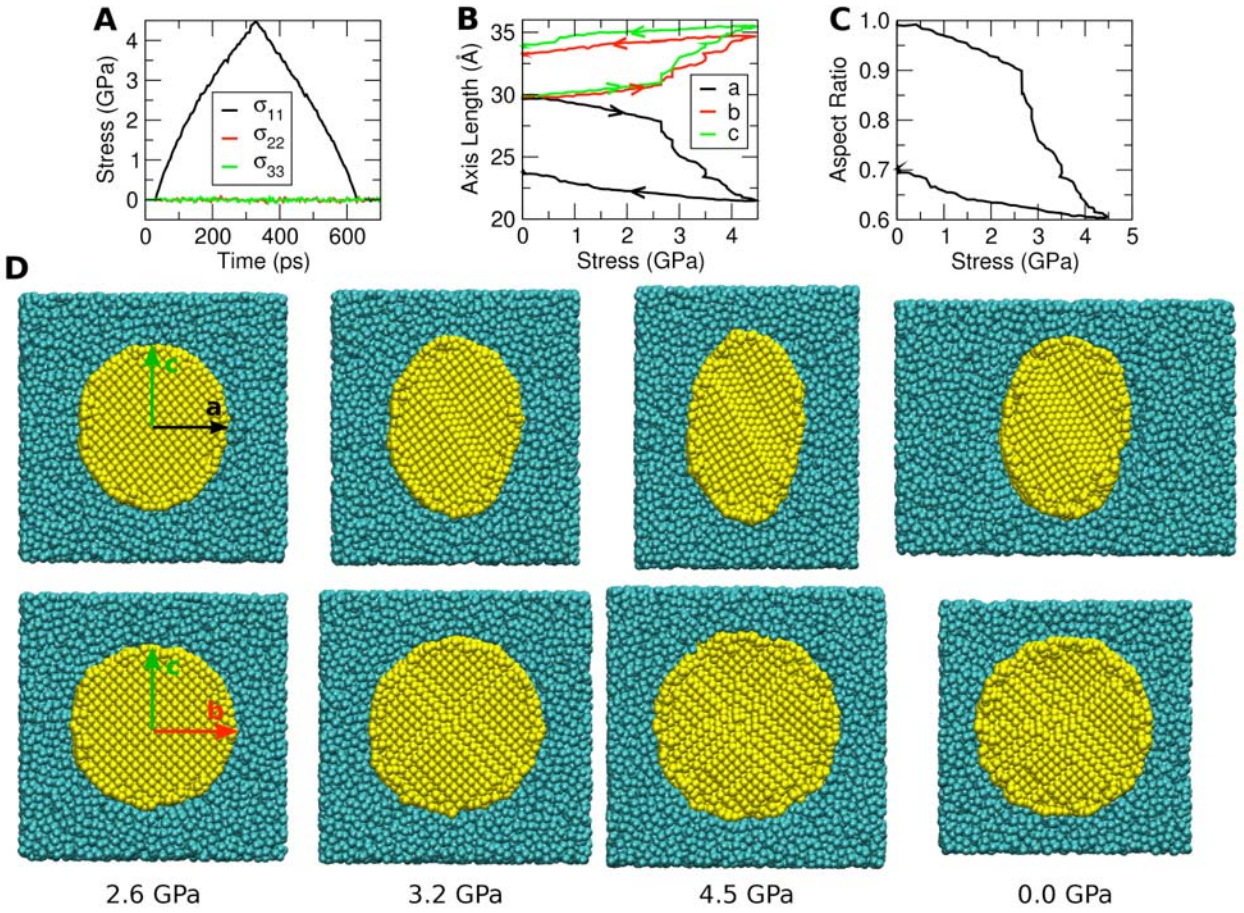

Figure 3.5. Irreversible shape change in a simulation of a 6 nm gold nanocrystal under uniaxial stress. (A) Diagonal components of the stress tensor as a function of time. (B) Semi-axis length of the ellipsoidal particle shape, as a function of stress, obtained from the principal moments of inertia of the gold particle. With increasing stress, the crystal transforms from a sphere to an oblate ellipsoid; the short axis a coincides with the direction of the stress. When the stress is released, the crystal shape remains strongly aspherical. (C) Aspect ratio a/c as a function of stress. (D) Time series of cross sections of the simulation box. In the upper row, the direction of the stress coincides with the semi-axis a, the lower row shows a view along the direction of the stress. Gold atoms are yellow, particles in the amorphous pressure medium are blue. At an upstroke stress of 2.6 GPa, the crystal is visibly deformed, but the interior crystal structure remains unchanged. Shape change is reversible up to this point, consistent with the smooth change of axis length in (B). At 3.2 GPa, the crystal has undergone slip relaxation and grain boundaries are visible. At 4.5 GPa, the minimal aspect ratio of 0.6 is reached and the stress is released again. When returned to ambient pressure, the crystal releases some elastic deformation but remains at an aspect ratio of 0.7, with most of the internal grain boundary structure intact.

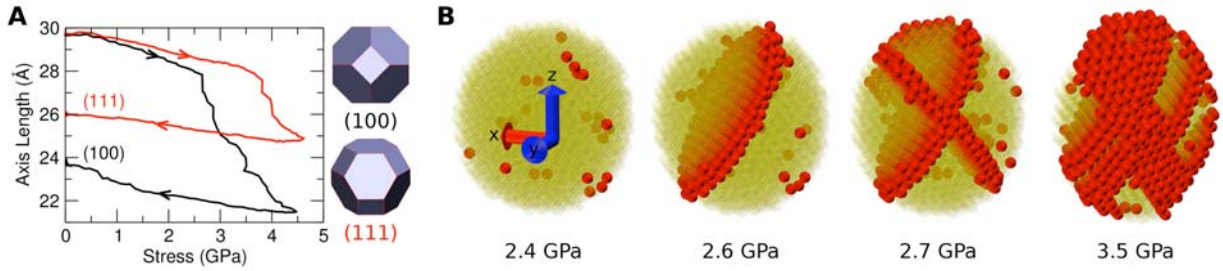

Figure 3.6 Shape change depends on particle orientation. (A) Short axis of two 6 nm crystals with different orientations with respect to the stress direction, as a function of applied stress. As illustrated by the polyhedral models, in the first crystal (black curve) the stress is applied in a [100] direction, in the second crystal (red curve) along a [111] direction. The first crystal begins slip relaxation at much lower values of the stress and undergoes a more dramatic overall shape change. (B) Mechanism of slip relaxation, illustrated in a series of snapshots of the (100) oriented crystal. Only gold atoms within a distance of 2.2 nm from the center of mass of the particle are shown. Atoms are colored according to their local environment: Atoms that have the same nearest neighbors as in the undeformed crystal are shown transparent yellow, atoms that have lost at least one of their original neighbors are colored solid red. Stress is applied in the x-direction, as indicated by the axis. At 2.4 GPa, the original crystal structure is intact. At 2.6 GPa, slip has occurred between two close-packed (111) planes. As the stress is increased (2.7 GPa and 3.5 GPa), slip continues between other (111) planes. At the highest applied stress, almost all original nearest-neighbor bonds have been broken.

The orientation of these particles with respect to the direction of shock propagation is thought to be the main source of ensemble broadening. The majority of plastic deformation events in nano-sized single-crystalline gold samples occur as a result of the formation of grain boundaries by the sliding of {111} planes. This is facilitated for particles oriented in the (100) direction, as the sliding occurs commensurate with the maximum resolved shear stress behind a uniaxial shock compression. That is to say that after the shock is inertially compressed to a highly uniaxial stress state, it is the direction that applies the most shear stress during the relaxation process to a more isotropically compressed state. Figure 3.6 shows that it is much easier to produce slip dislocations in a particle that is oriented such that the {111} planes are oriented ~45^{o} with respect to the direction of shock propagation, which is the angle commensurate with the maximum shear stress applied by the shock [2].

One other factor that would contribute to lowering the barrier for deformation is the presence of twin boundaries in particles of this size. These have been shown to exist in larger gold clusters, like the ones studied in this work. The simulations do not include this effect, and thus the onset of plastic deformation is calculated to be higher than what is observed experimentally (<1 GPa). Grain boundaries present in nanoscopic objects have been shown to lower the onset of slip dislocations to ~0.1 GPa [40]. This is lower than our experimental resolution and far below the maximum pressures we achieve.

3.4 Conclusions

The SPR band shifts to higher energies when pressurized. This is most likely due to an increase in Fermi energy and unequal band-spreading of the s and d conduction and valence bands, respectively, near the Fermi energy. This should be offset by any increase in the media's dielectric, but the material is much less compressible than in past studies in liquids. Thus, whatever effect the polymer's dielectric is having, it is more than offset by the shift induced by the change in the gold particles' electronic structure.

Commensurate with the blue-shift of the primary plasmon peak, a new peak to the red appears. This represents the fraction of particles in the ensemble being deformed behind the

shock front. It is broader than the electrostatic calculations predict, due to the initial orientational polydispersity of the ensemble. This, in addition to the small distribution of sizes in the sample contribute to the size polydispersity of the resulting spheroids, the response of which is exponentially dependent upon the particles' aspect ratio.

Both peaks have the same dynamics as the incident pressure wave in that they are coincident with the arrival of the shock front and they do not change after shock arrival. That is to say that there is no lag in time between the compression and distortion events observed in the sample observed.

There is good qualitative agreement between the experimentally observed behavior of the particles under shock compression and the simulations presented. These results show, for the first time, a direct observation of the effect of density increase on the optical properties of gold nanoparticles. The splitting of the plasmon resonance into two distinct peaks shows the result of a uniaxial compression characteristic of a shock wave.

Chapter 4:

Shock-Induced Phase Transition of Cadmium Selenide Nanocrystals

4.1 Introduction

Structural phase changes play an important role in processes ranging from polymorphic transformations during geological events to the production and tempering of steel [40]. They have also garnered recent interest due to the applicability of phase change materials to nonvolatile storage media [43,44]. Various techniques have been developed to study the dynamics of such phase changes. For example, ultrafast x-ray spectroscopy has been used to examine the dynamics of phase transformations induced by optical pulses [45]. Also, shock waves can provide a means of rapidly increasing the pressure on a sample, using ultrafast optical pulses to follow the resulting structural changes [46-48]. The limitations arising from the use of bulk samples, however, are numerous, owing to the complex transformation kinetics that arise when multiple, uncorrelated, nucleation events occur [43].

Following nucleation, an individual nanocrystal, on the other hand, transforms completely within 10 ps, based on recent simulations [50,51]. Since nucleation is a rare event under hydrostatic compression near the transition pressure, a second nucleation event occurring during that short transformation time is unlikely, and is therefore not observed for nanocrystals compressed in a diamond anvil cell (DAC) [52]. In a DAC this leads to simple kinetics for the ensemble of nanocrystals, relative to those observed for bulk systems. As an example, the wurtzite-rocksalt transformation kinetics have been studied for 4 nm CdSe nanocrystals in a DAC, and the temperature and pressure dependent rate constants are observed on time scales of 10 ms and longer [49,53]. These slow ensemble kinetics obscure the dynamics in individual nanocrystals. In a shock wave experiment involving hard nanocrystals embedded inside a soft polymer, the pressure around each nanocrystal can rise on a similar time scale as that for a sound wave to traverse the entire nanocrystal. Therefore, shock wave experiments on nanocrystals can potentially reveal aspects of the transformation mechanism that cannot be discerned from further DAC studies.

In a DAC the small size of CdSe nanocrystals leads to further discrepancies in behavior between nanoscale and bulk crystals during the wurtzite-rocksalt phase change [52]. For instance, in 4 nm diameter CdSe nanocrystals, the theoretical thermodynamic transformation pressure, P_{therm}, at which the wurtzite and rocksalt crystal structures are isoenergetic, is elevated (P_{therm} ~2.3 GPa) from the bulk value ($P_{therm,bulk}$ ~ 2.0 GPa). There is also a larger kinetic barrier in the case of nanocrystals than in the bulk, leading to a broad hysteresis between the experimentally observed transformations in the forward (P_{fwd} ~ 7 GPa) and reverse (P_{rev} ~ 1 GPa) directions.

The effect of shock compression on CdSe nanocrystals embedded in a polymer matrix is studied here. A reduction of the upstroke transition pressure 3.2 GPa of P_{fwd}, and a large increase in the transformation rate relative to DAC experiments consistent, at the highest pressures studied, with multiple nucleation events occurring per particle.

4.2 Experimental Methods

4.2.1 Sample Preparation

High-quality spherical CdSe nanocrystals 4.0 nm in diameter (relative standard deviation = 5%) were colloidally grown using the Murray method [54]. The shock wave generation method used was adapted from the work of Dlott and utilizes a pulsed laser to produce shock waves via the rapid partial ablation of a thin metal film [47,3]. Shock targets [Fig. 4.1(a)] were assembled from 200 μm thick CorningTM 0211 glass, vapor coated with 1.5 μm of aluminum. A 1 μm thick (5%) polyvinyl(butyral-co-vinyl alcohol-co-vinyl acetate) (PVB) buffer layer was spin coated from chloroform solution on each target and cured at 120 ^{o}C for 30 min. Next, a 250 nm (10%) sample layer, containing either 8 wt % rhodamine 640 perchlorate dye (R-640) in PVB as a pressure probe or 5 vol % CdSe nanocrystals in PVB was spin-coated. An overlayer of 5-min epoxy was applied, followed by cover glass.

4.2.2 Spectroscopic Technique and Apparatus

The regeneratively amplified Ti:sapphire laser system used here produces 1 mJ pulses with a central wavelength of 800 nm. The uncompressed shock-generation pulse (200 ps, 900 μJ) was focused to a 250 μm diameter spot on the rear of the target [Fig. 4.1(a)]. Since the aluminum shock-generation layer was damaged by the pulse, the target was mounted on a translation stage to expose a fresh area for each shock. A compressed pulse (50 fs) was used to generate a broadband continuum probe in a sapphire crystal. The probe beam was focused to an 80 mm spot and reflected normal to the remaining aluminum layer. The absorption spectrum at each time delay, collected with a charge coupled device, consisted of a software averaged row of ~100 shocked spots. A background correction was performed on each spectrum by subtracting the absorption of a blank target under the same shock conditions.

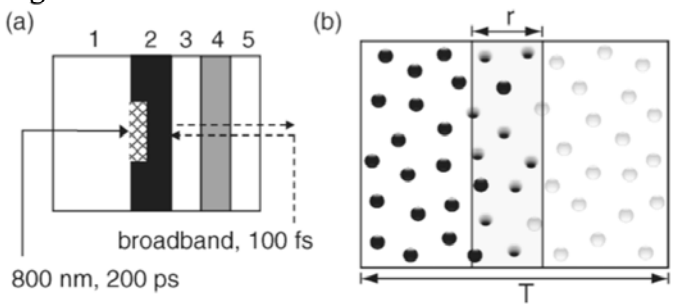

Figure 4.1: (a) Target cross section schematic: (1) glass; (2) aluminum with ablated portion (crosshatched); (3) PVB buffer layer; (4) sample layer containing CdSe, R-640, or PVB only; (5) epoxy overlayer. (b) Detail: Sample layer of thickness T with wurtzite (white), rocksalt (black), and partially transformed (gray) CdSe nanocrystals. r is the shock front propagation per unit time. (Not to scale).

4.3 Results and Discussion

We have produced shock waves yielding peak pressures ranging from 2.3 to 3.75 GPa. The pressure corresponding to each particular pump pulse energy was determined by loading the sample layer with R-640 dye, whose absorption feature redshift ($\Delta\lambda$) as a function of pressure has been previously characterized [47]. Our $\Delta\lambda$ is plotted in Fig. 4.2 as a function of time for three different pump pulse energies.

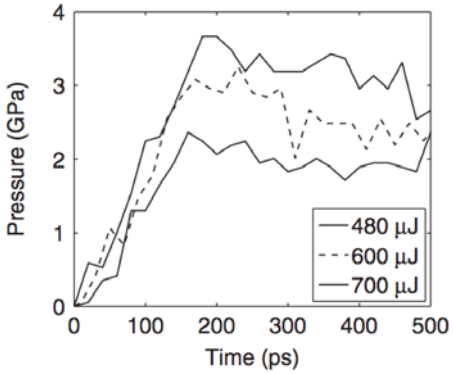

Figure 4.2: Shock pressure, from R-640 Δλ (1 GPa ~ 4 nm redshift), at multiple pump pulse energies.

The pressure in the R-640 layer rises within 200 ps, after which it remains stable for 200-300 ps. The single rise indicates the lack of a reflected shock through the sample layer at any pressure examined. The front of a 3 GPa shock should move at 3-6 nm/ps, traversing the 250 nm sample layer within 70 ps [39]. The longer 200 ps rise time is due to the viscoelastic response of the polymer matrix containing the R-640, a two-stage process consisting of an instantaneous uniaxial elastic compression, followed by a slower relaxation to a plastically deformed state exhibiting a more hydrostatic pressure [3].

The behavior of CdSe nanocrystals under shock compression is shown in Figs. 4.3(a)–4.3(c). Their corresponding behavior under hydrostatic compression in a DAC is shown in Figs. 4.3(d)–4.3(f). The optical spectra in Figs. 4.3(d)–4.3(f) have been correlated with x-ray data [52]. When shocked to 2.3 GPa [Fig. 4.3(a)] there is a blueshift, as well as a decrease in optical density (OD) of the first excitonic absorption feature. The blueshift is due to elastic compression of the CdSe wurtzite lattice, which increases the band gap energy (E_{gap}) [Fig. 4.3(d)] [55]. The decrease in exciton peak intensity during the first 100 ps is the result of thermal broadening. After 100 ps, as the polymer begins to relax and the nanoparticles experience a more hydrostatic environment, E_{gap} shifts.

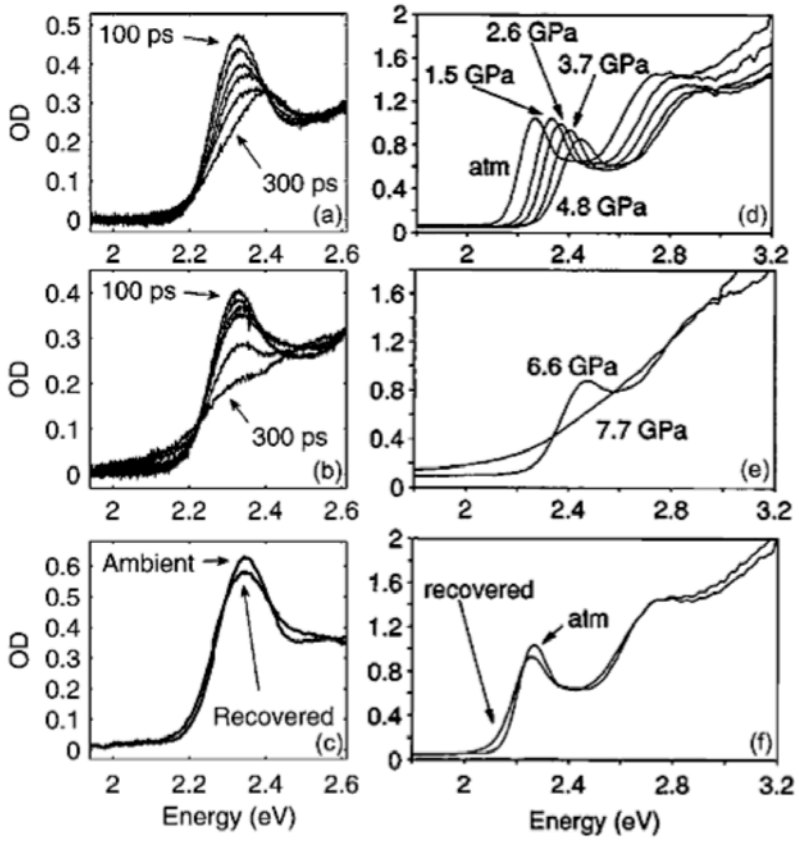

Figure 4.3: Spectra of CdSe nanocrystals under shock compression by a 2.3 GPa shock (a), and a 3.2 GPa shock (b). Δt between spectra is 50 ps. Panel (c) shows the recovered spectrum many minutes after the shock has passed (averaged over the entire target area). At right, (d)-(f) are the corresponding spectra of CdSe nanocrystals under slow, hydrostatic compression.

When shocked to 3.2 GPa [Figure 4.3(b)], there is also an initial reduction in exciton peak intensity (0–200 ps), without a shift in E_{gap} . At 200 ps, however, there is a precipitous drop in exciton peak OD and E_{gap} remains unshifted, despite the more hydrostatic environment. The lack of a shift indicates that the particles are no longer in the wurtzite phase, which would exhibit a shift in E_{gap} under hydrostatic compression. It may also suggest transformation from the plastic state, with plastic deformation preceding the phase change [48]. Additionally, a broad tail develops to the red of E_{gap}, characteristic of indirect narrow-gap rock-salt CdSe. Some nanocrystals remain untransformed, leading to a small residual absorption near the wurtzite E_{gap}. Though thermal broadening affects the peak OD prior to the transformation, the temperature rise estimated in the literature for shocks of 2–4 GPa is 150 ^{o}C, which would not, by itself, bring about the observed above 3 GPa [47,3].

Further evidence for the transformation is provided by the transient behavior of the optical spectra (Fig. 4.4). With a 2.3 GPa shock ΔOD/OD, at E_{gap} for each spectrum, reaches a steady value near 100 ps. These are qualitatively the same dynamics observed in the R-640 target, indicating that nanocrystal spectral changes are tracking closely with the polymer compression. With a 3.2 GPa shock, however, a second large jump in ΔOD/OD, not observed in the R-640 experiments, occurs after 200 ps. We assign this change in the nanocrystal spectrum, decoupled in time from the polymer relaxation, to the structural transformation of the nanocrystals from wurtzite to rocksalt. The secondary rises in signal from 3.2 and 3.75 GPa shocks begin at similar

values of ΔOD/OD to the maximum value reached due to a 2.3 GPa shock, indicating the limit of thermal broadening prior to transformation.

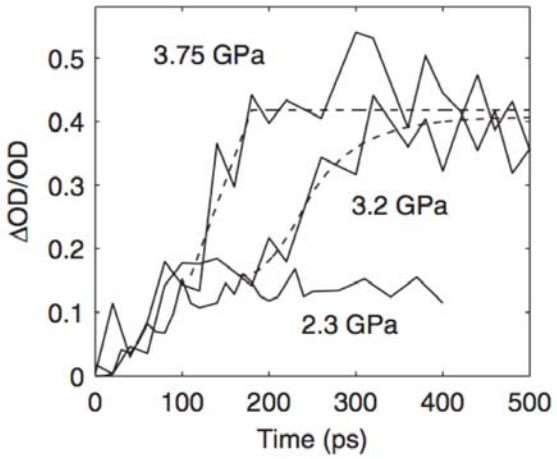

Figure 4.4. Change in CdSe peak OD versus time at various peak shock stresses. The dashed lines indicate fits to the data, described in the text.

There is an induction period of 90 ps between the stabilization of the polymer dynamics and the onset of the transformation, explained by Gupta and co-workers as the time required to grow a sufficient number of stable nuclei from the spontaneous local fluctuations between phases that occur near the transformation pressure [48]. The absolute induction times observed here are much shorter than in that work (90 ps versus 3 ns) because here the transformation dynamics are convoluted with a shock transit time across a much thinner sample layer (250 nm versus 250 m). The relationship between critical nucleus size and applied pressure has been studied for CdSe nanocrystals in recent simulations [56]. The critical nucleus size decreases with increasing pressure, so the induction time should decrease as a function of applied shock stress in the case of CdSe nanocrystals, as observed for bulk CdS in Gupta's work. In fact, following a 3.75 GPa shock (Fig. 4.4), the induction time becomes much shorter and the signal rise steepens.

The observed behavior differs from that under slow, hydrostatic compression. Under shock compression the transformation (~3 GPa) occurs above P_{therm} (2.3 GPa) but well below the upstroke pressure P_{fwd} required in a DAC (~7 GPa). Using the kinetic data derived from the DAC experiments, we can conclude that under hydrostatic conditions, at 3 GPa and 150 ^{o}C, the structural transformation would not have any possibility of occurring on the timescale of these experiments (Table 4.1). In fact, under hydrostatic compression, an ensemble of nanocrystals brought above its transition pressure within a few seconds has a half-life for transformation of tens of microseconds even at 500 ^{o}C [49,53].

P (GPa)	T (K)	ln(k)	t_{rel} (s)	t_{rel} (h)
2.1	463	−14.56	1.46×10^{6}	405.38
2.1	673	3.60	1.89×10^{-2}	
2.1	753	7.73	3.05×10^{-4}	
3.0	463	−12.44	1.75×10^{5}	48.74
3.0	673	5.06	4.40×10^{-3}	
3.0	753	9.03	8.29×10^{-5}	

Table 4.1. Relaxation times ln(2)/k (half-life) for wurtzite-rocksalt phase transformation of CdSe nanocrystals in DAC kinetics experiments. Distilled from Refs. [47,51].

Under shock compression, in addition to a small reduction in P_{fwd} by the elevated temperature, the anisotropy of the applied pressure facilitates and expedites the structural transformation as compared with hydrostatic DAC compression. A higher effective stress is experienced by the shocked nanocrystals due to the initial uniaxial compression of the sample, resulting in shear stresses described by Equation-4.1:

$$p_z = \bar{p} + \frac{4\tau}{3}$$

where τ is the maximum resolved shear stress along planes with normal unit vectors at 45° relative to the applied stress, p_z [46]. The R-640 experiments measure the mean isotropic stress $\bar{p}$, analogous to the pressure P in static DAC experiments, since R-640 is a small molecule insensitive to shear. Crystalline materials, however, should experience the applied stress as p_z . Bulk CdS has been shown to transform at a lower pressure under shock compression than under hydrostatic compression, with a value for $4\tau/3$ of ~1 GPa [57]. τ may be as high as 2 or 3 GPa for nanocrystals to account for the difference in P_{fwd} between shock and DAC experiments, though it is difficult to determine precisely, since the geometry of the nanocrystal-polymer composite may complicate the stress-strain history of each nanocrystal. A greater susceptibility of nanocrystals to shear is consistent with their single domain character. Shear strain can extend in a single direction through an entire nanocrystal, without encountering the crystalline domains of disparate orientation that are present in bulk crystals during the phase transformation [42,48]. The more rapid kinetics observed under shock compression than in a DAC further imply a reduction in the kinetic barrier to transformation. Since martensitic phase transformations, such as wurtzite-rocksalt, exhibit nucleation dependent kinetics, this implies more facile nucleation. Martensitic transformations are characterized by a well-defined mechanism dominated by the shearing of crystal planes with respect to one another [42]. An applied stress that induces shear strains, as is present under shock compression, effectively catalyzes the transformation by driving the crystal atoms preferentially along the reaction coordinate. Additionally, since the applied shock stress is near the Hugoniot elastic limit for CdSe, some degree of plastic yielding is expected, which may further facilitate the transformation if it occurs along relevant crystal planes [46].

The transients in Fig. 4.4 have been fit to a model proposed by Turnbull for the phase transformation of a sample divided into small ‘‘droplets’’ [58]. Each droplet is assumed to undergo only one nucleation event during the transformation time and, following nucleation, the new phase grows at a constant rate, and for a short time limited by the droplet size. Since these assumptions match the known behavior of nanocrystals [52], Turnbull’s model has been adopted,

modified to account for the shock transit time across our sample layer. The phase transformation kinetics of the ensemble of droplets are dependent upon the nucleation rate, and can be described by Equation 4.2:

$$V(t) = \sum_{i=1}^{T/r} \frac{V_o}{T/r}\left[1 - \exp\left(-Iv\,\frac{(t-i)) + |t-i|}{2}\right)\right]$$

where *T* is the total thickness of the sample layer, and r is the shock propagation rate [Fig. 4.1(b)] [58]. Each coarse-grained slice is shocked sequentially. *V(t)* is the absolute volume of transformed material at time *t*. I is the nucleation rate per unit volume and *v*, the droplet size, is 33.5 nm^3 for 4 nm diameter nanocrystals. V_0 is the total volume of CdSe in the probe area. The data have been fit to $fV(t)/V_0$, the fractional volume transformed. *f* is a normalization factor accounting for the fact that ΔOD/OD is not expected to reach unity even upon full conversion.

4.4 Conclusions

Fits to the 3.2 and 3.75 GPa data yield values for the absolute nucleation rate per slice, $\frac{IV_o}{T/r}$, of 8.6 x 10^5 ps^{-1} and 2.7 x 10^8 ps^{-1}, respectively. Within the probe area there are ~5.4 x 10^7 nanocrystals in each 4 nm slice of the sample layer, the approximate thickness traversed by the shock wave each picosecond. Therefore, a nucleation rate per slice greater than 5.4 x 10^7 ps^{-1}, as is the case for the 3.75 GPa shock, suggests more than one nucleation event per nanoparticle. Simulations of the zinc-blende to rocksalt phase change in GaAs nanocrystals, which reach the transformation threshold on a similar time scale as in our experiment, have also been shown to exhibit multiple nucleation events [59].

In summary, we have observed a more facile and rapid transformation between the wurtzite and rocksalt crystal phases in CdSe nanocrystals under shock compression than observed in a DAC. Under shock compression, the nucleation rate approaches the rocksalt phase growth rate, allowing multiple nucleation events per nanocrystal. Time-resolved x-ray experiments are required to directly observe these nanocrystal structural dynamics.

Chapter 5:

Attenuation of Shockwaves Using Hollow CdS Nanoparticles

5.1 Introduction

Due to their small size, it is unlikely, given a macroscopic stress, that the small (1-14 nm diameter) nanospheres discused in chapter 4 would fracture into smaller pieces. The increase in particle free energy brought about by the resulting increase in surface area would be prohibitive. Fracture has been observed upon applied stress, however, in much larger nanocrystals, specifically long CdSe nanorods and hollow CdS nanospheres [60,61]. In CdSe nanorods, the observed fracture is ascribed to the formation of domain boundaries during the transformation, at which interfacial strain energy builds to the eventual point of fracture. The strain is the result of the macroscopic morphological deformation that accompanies the phase transformation, causing a lateral displacement of the rod in the transforming region. The topological distortion of the rod-shape through the phase transition is thought to lead to a kinking process that is resisted by the hardened pressure–transmitting matrix. As a result, the phase transition in rods of a significant aspect ratio is accompanied by fracture. This morphology change was discussed in chapter 5 and is the result of the martensitic nature of the transformation.

Hollow nanospheres are created from the sulfidation of cadmium spheres via the nanoscale Kirkendall effect, whereby the asymmetric diffusion rates of the anion and cation to the reaction zone between the two materials leads to the formation of voids inside the material. At the nanoscale, these voids are in such close proximity that they are able to coalesce to a single hollow at the center of the particle within the timeframe of the reaction [62]. A typical sample of hollow nanospheres is depicted in the micrographs of Fig. 5.1. Some of the samples used in the experiments described in this chapter were provided by Dr. Andreu Cabot. The rest were synthesized in a manner identical to the one described with in the preceding reference.

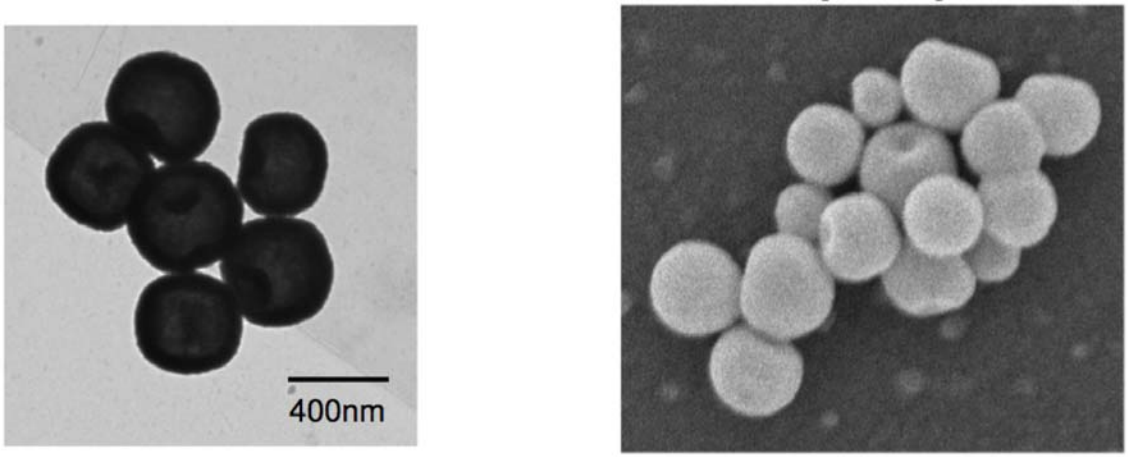

Figure 5.1: The as-synthesized hollow CdS nanoparticles. (a) Transmission electron micrograph, (b) Scanning electron micrograph. Particles provided by Dr. Andreu Cabot.

Hollow CdS nanocrystals are larger than the particles described in the preceding chapters and contain multiple crystalline domains. Though they are not single crystals, their domains are quite small, a few nanometers in size. According to the Hall-Petch relation, the yield stress for a crystalline macroscopic material is inversely proportional to the size of the grains of which it is comprised. Hollow nanocrystals have therefore elicited interest as shock absorbers, since they will support a large applied stress and undergo a large strain prior to their ultimate fracture. This behavior has been studied previously using a diamond punch apparatus coupled with transmission electron microscopy (TEM) [60]. By combining those experimental methods with finite-element analysis, the maximum shear stress supported by the hollow nanospheres was calculated in that work to be 2.2 GPa. *

The fracture of hollow CdS nanospheres has been affected using laser-induced shock waves in order to determine their ultimate suitability as shock absorbers. Shocked samples have been recovered and examined using transmission electron microscopy. A time-resolved experiment to measure the attenuation of the incident shock energy upon traversing a layer of hollow nanospheres has also been performed. This experiment involved measuring the pressure achieved in an R-640 pressure probe layer downfield of the sample layer containing the hollow nanospheres. The peak pressure was compared to that achieved after the shock had traversed a "blank" polymer, layer devoid of nanocrystals.

5.2 Experimental Methods

Hollow CdS nanocrystals, were synthesized using the method of Yin, et al. [62,63]. These nanocrystals were characterized using optical absorption, fluorimetry and transmission electron microscopy (TEM). The nanocrystals were determined to be ~400 nm in outer diameter, with a shell-thickness of ~50 nm.

5.2.1 Sample Preparation

Shock targets [Fig. 5.2(b)] were assembled from 1 inch diameter, 200 μm thick, Corning™ 0211 glass wafers, vapor coated with 1.5 μm of aluminum (Cascade Optical Corp.). A 1 μm thick (±5%) polyvinyl(butyral-co-vinylalcohol-co-vinyl acetate) (PVB, Aldrich) buffer layer was spin-coated from chloroform solution on each target. The purpose of the buffer layer is to allow the shock front time to steepen prior to reaching the sample. If the buffer layer is too thick, however, (>6 μm) a significant portion of the shock energy will have dissipated prior to reaching the sample [37]. Buffer layers were cured at 120 ^{0}C for 30 minutes to cross-link the polymer chains, reducing their solubility in chloroform in order to prevent dissolution of the buffer layer during sample layer application. Next, a 400 nm (±10%) sample layer, containing 30 or 60 vol.% CdS hollow nanospheres in PVB was spin-coated from chloroform solution. The lower limit to the thickness of the sample layer is the diameter of the nanoparticles, ~400 nm. A probe layer was spin-coated next, which contained 8 wt.% Rhodamine 640 Perchlorate dye (R-640, Exciton) in PVB. An over-layer of 5-minute epoxy (Devcon™) was applied, and flattened with a layer of cover glass to remove air pockets and protect the entire multi-layer structure. Layer thicknesses were determined using a KLA-Tencor Alpha-Step IQ profilometer. Thickness error was determined by measuring many areas of each layer.

* It should be noted that these values are only strictly valid for a geometry in which the stress is applied between two parallel plates.

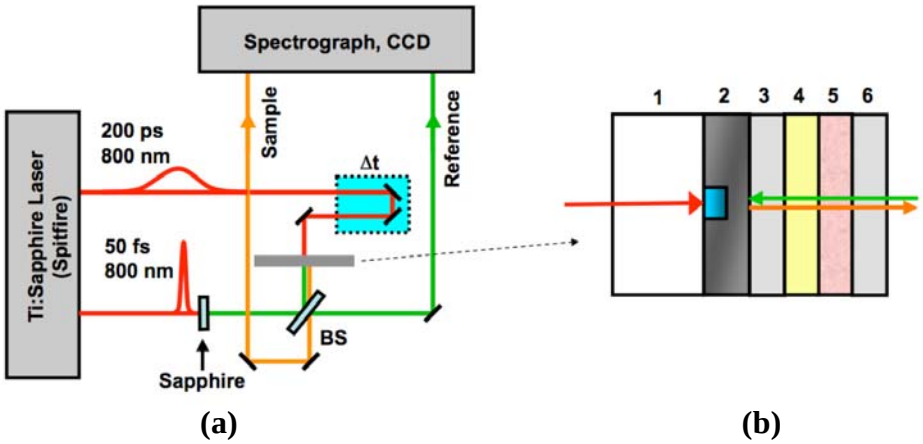

Figure 5.2: (a) The transient shockwave apparatus, (b) the sample cross-section schematic showing: 1. Corning 0221 glass substrate, 2. 1.5 micron aluminum layer, 3. PVB buffer layer, 4. Shock attenuation layer, 5. Shock measurement layer (R-640 dispersed in PVB), 6. Devcon™ Epoxy and glass over-layer.

5.2.2 Ultrafast Spectroscopic Techniques

A background correction was performed on each spectrum by subtracting the absorption of a blank target, i.e. one with the same multilayer structure, under the same shock conditions, but without R-640 or CdS hollow nanospheres added to the sample and/or pressure probe layers. The peak red-shift ($\Delta\lambda$) of the R-640 absorption feature was compared between R-640 layers with and without hollow particles loaded into the sample layer preceding them.

5.2.3 Recovery and Electron Microscopy of Shocked Particles

For electron microscopy analysis of recovered particles, the sample layer was dissolved, using chloroform, from the target subsequent to shock compression. The resulting chloroform solution remained dilute and did not undergo a precipitation step to attempt concentration of the recovered nanoparticles. While multiple controlled precipitation cycles are generally used to remove excess organic material from nanoparticle solutions, the amount of nanocrystal sample being recovered was so small that processing was minimized to avoid its loss. Nanocrystals were deposited onto copper mesh TEM grids directly from the original solution.

5.3 Results

5.3.1 Electron Microscopy of Fractured CdS Nanospheres

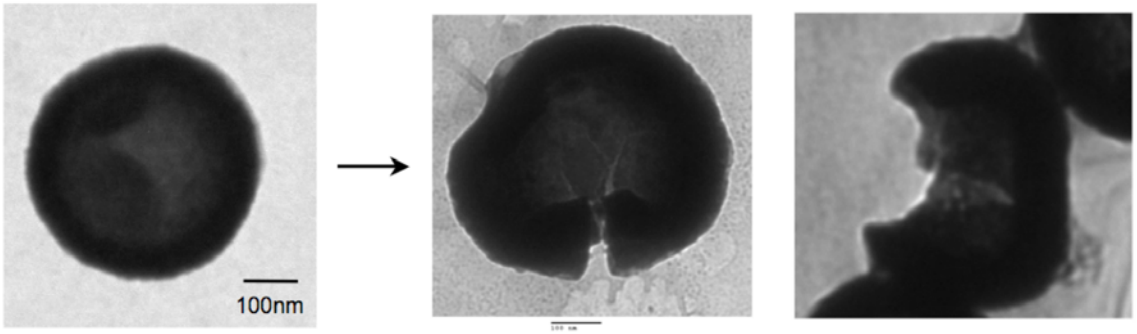

(a) **(b)**

Figure 5.3: CdS nanoparticles recovered from (a) an unshocked sample and (b) from a sample that has undergone shock-compression.

Fractured nanocrystals are depicted in Fig. 5.3. At left (a) is a nanoparticle that has experienced the entire processing cycle of spin coating, curing and dissolution, but not shock compression. At right (b) is a pair of images illustrating the result of shock compression. The analysis of recovered particles, unfortunately, could not be performed on samples that had undergone shock compression in a target structure containing all of the layers necessary for the R-640 pressure measurement. The sheer abundance of polymer, by mass, in the targets, relative to the amount of sample present, was simply too large. Rather, these samples were recovered from a target comprised only of buffer and sample layers.

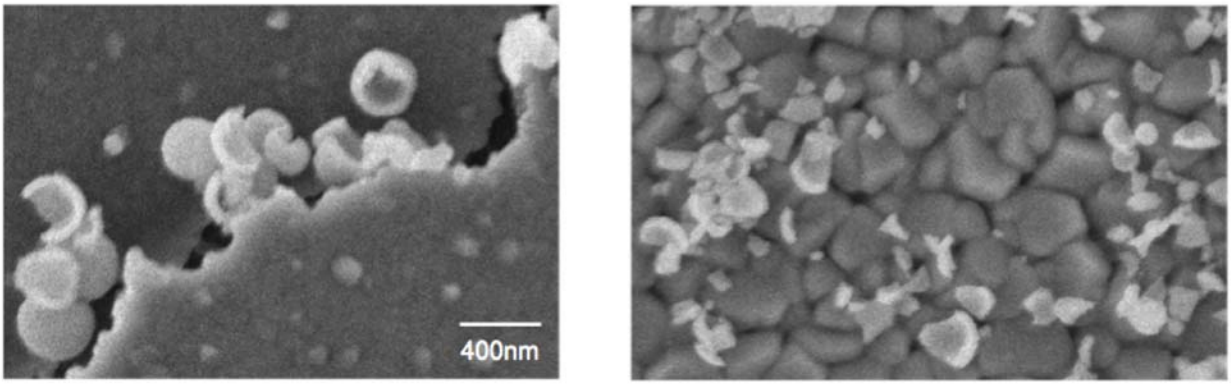

(a) **(b)**

Figure 5.4: Scanning electron micrographs of hollow CdS nanospheres recovered following shock-wave compression. (a) nanoparticles after shockcompressioninducedbya120 μJ laser pulse. (b) nanoparticles after shock compression induced by a 160 μJ laser pulse.

Fig. 5.4 shows SEM images of fractured particles. In order to image the smaller fragments without the interference of polymer detritus, these samples were deposited from chloroform solution directly onto the aluminum shock generation layer, and imaged without further processing. It is clear that, there is a qualitatively greater degree of fracture in the particles shown in Fig. 5.4(b) illustrating that, following a shock generated by a 120 μJ laser pulse, the majority of the observed fragments are almost-complete spheres or small pieces, indicating that on

average the spheres were chipped, with small pieces having been broken off, but have remained mostly intact. The majority of particles has been multiply-fragmented, with very few large pieces remaining. The inability to combine electron microscopy with targets constructed from multiple polymer layers precludes the comparison of the applied pressure and its effect on the nanocrystals in a quantitative manner, by TEM or SEM.

5.3.2 Attenuation of Transmitted Shock Stress by CdS Nanospheres

Figures 5.5, 5.6, and 5.7 illustrate the results of time-resolved studies on shock-compression of hollow CdS nanospheres that were performed. The pressure in the R-640 probe layer rises as a result of the shock compression, as determined by the shift, $\Delta\lambda$, of the R640 absorption feature, the pressure dependence of which has been studied previously and is 4 nm/GPa. The shock wave, as discussed in Chapter 1, traverses the R-640 probe layer within ~70 ps. A response any longer than that is caused by the relaxation dynamics of the polymer matrix in which the R-640 is dissolved, as long as the shock itself has not been disturbed while traversing the target layers preceding the R-640 probe layer.

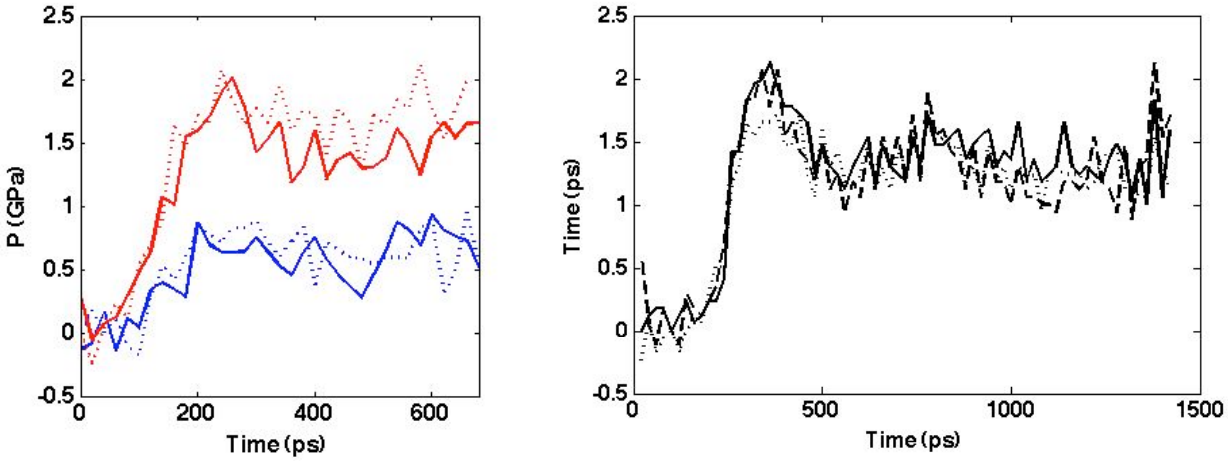

Figure 5.5: Shock transients for shock waves that have traversed different sample layers containing CdS (dashed) and ones that were exclusively made up of polymer (solid) for (a) two different shock stresses 0.6 GPa (blue) and 1.5 GPa (red); and (b) at different loading densities: Pure PVB (solid), 30% v/v CdS (dashed), 60% v/v CdS (dots).

When a shock of low strength is incident upon the attenuation layer, it exhibits a pressure transient that is, for all intents and purposes, identical to a shock of the same strength that is allowed to propagate through a pure polymer layer, as in Fig. 5.5(a). In Fig. 5.5(b), the shockwave is shown to be independent of loading density of the CdS nanoshells, so long as the stress incident on the sample is below ~1.5 GPa. At higher incident stresses, attenuation of the shock is observed, as shown in Fig. 5.6(a). In the samples shocked at peak pressures between 1.5 and 3 GPa, the pressure transmitted through the CdS-PVB composite does not exceed 1.5 GPa [Fig. 5.6(b)].

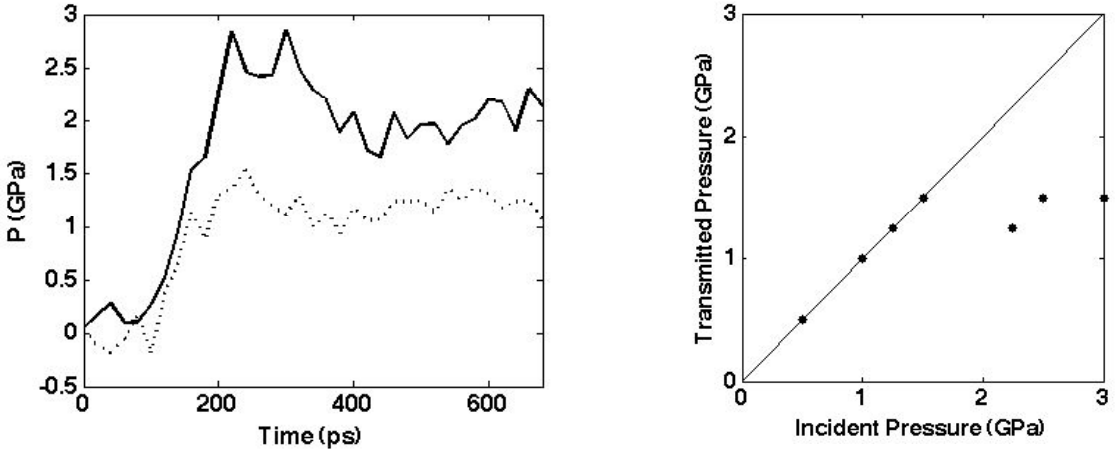

Figure 5.6: Shock waves that have passed through a sample containing (a) CdS (dashed) and one that contains only polymer (solid) show different pressure transients. (b) maps the pressure transmitted through a composite layer of CdS particles in PVB against the pressure transmitted without the shock-absorbing shells.

In Fig. 5.7(c), the pressure rise in the R-640 layer upon shock compression to 3.75 GPa is depicted. At this peak pressure, the behavior of the R-640 layer with CdS hollow nanospheres preceding it is quite similar to the behavior when no hollow spheres are present.

This was a surprising observation, considering that the stress, as mentioned previously, required to break a hollow nanosphere is ~1/2 GPa. The shock pressure incident on the hollow spheres is at least an order of magnitude greater than that, and so the particles should almost certainly be fracturing. However, taken as a percentage of total applied energy, it is possible that the energy absorbed by the nanoparticle layer is below the limit of the experimental resolution. Additionally, it is important to note the difference in rise-times between the highest stress case and the rest of the data.

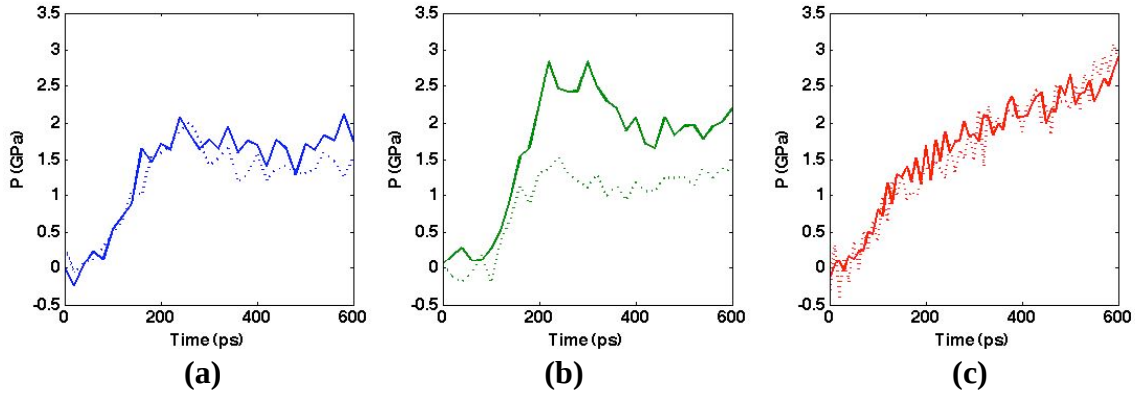

Figure 5.7: Shock transients for samples with attenuation layers containing CdS (dashed) and those only containing PVB (solid). (a) Shows no difference between the two while (b) shows that there is significant attenuation of the shock by the particles, and (c) shows qualitatively different behavior of both the pure polymer and the CdS-PVB relative to the others. (The data from Fig. 5.6(a), is replotted here in Fig. 5.7(b) for comparison).

The small chips removed from fractured hollow spheres at lower applied stresses (c.f. Fig. 5.4(a)) may represent regions where particles were touching each other or the Al surface, in the case of the experiment performed without polymer present, leading to localization of shear strains in those areas. Localization of shear strains in the contact area between the tip and the

nanocrystal shell wall was observed in the diamond punch hollow nanosphere fracture experiments [60]. This also agrees with observations of the compression millimeter sized hollow metallic spheres, which show preferential fracture at sinter necks between adjacent particles, or else at defective regions of the sphere wall, which cause the removal of small fragments from the spherical shells [61].

The slower rise time of the pressure in Fig. 5.6(c) as compared to the lower stress transients points to a long-lived relaxation process in the film [1]. Such behavior has been observed in polymer and polymer-protien films by Dlott and co-workers. [63] The total shock Hugoniot curve for the polymer composite may not be qualitatively different above V_o, as discussed in Chapter 1. The shear relaxation of the polymer matrix would then place across the front of the shock, lengthening the observed rise-time [1].

This may also be the result of multiple fracture, a slower process overall than simple pore fracture, occurring at higher applied stress, such as that observed in Fig. 5.7(c). Fewer fracture events per particle at lower applied stress, as observed in Fig. 5.7(b), may lead to a more rapid transmission of the shock energy to the probe layer. A longer duration the pressure rise in an R-640 probe layer resulting from the compression of hollow nanopores has been observed previously [78] In that work, the pores collapsed by a radial viscoplastic collapse mechanism with a time constant of over 300 ps. Viscoplastic collapse of the polymer surrounding the CdS hollow naospheres would only be possible in the case of extensive fragmentation. With few fractures per particle, the fracture event should have a smaller effect on the overall timescale for pressure transmission to the probe layer. Significant effects, such as these, on the dynamics of shock wave propagation resulting from the microstructure of the sample in shock experiments have been described previously [64].

5.4 Conclusions

The fracture of hollow CdS nanospheres under the influence of shock compression has been observed. Nanospheres undergo few fractures per particle in the case of low incident instantaneous stress, whereas they are multiply-fractured in the case of higher instantaneous stress. A polymer layer containing hollow nanospheres has been shown to cause attenuation of applied shock stresses >1.5 GPa. Which is, in general, in agreement with the results of previous work. The greater degree of fragmentation in more strongly shocked hollow nanospheres may lead to a different mechanism for shock propagation than in less strongly shocked samples, as evidenced by the longer timescale for pressure rise in the R-640 layer at higher applied shock stress.

Additional experiments are needed to refine and further justify these conclusions. Multiple loading densities of hollow shells probed above the 1.5 GPa threshold for attenuation may confirm the hypothesis of multiple fracture, as it would allow for larger energy absorption overall. Experiments involving particles with variable shell thicknesses would also give valuable information to the origin of the threshold stress for energy absorption.

Chapter 6:

Future Directions

The techniques described herein have probed the structural and mechanical behavior of materials indirectly, using time-resolved optical spectroscopic techniques. While the electronic structure is dependent upon the details of how the atoms in an analyte are ordered, there are serious limitations to using electronic structure to learn about the atomic ordering in a material. The most severe limitation is that in order to probe a material by optical spectroscopy, the material must have an optical resonance that is able to report something useful about the structure of the material in question. The choice of CdSe for studying the dynamics of polymorphic phase transitions was based, in no small part, on the transition being between that of a direct-gap (the band-gap transtion is vibronically allowed) and an indirect-gap (a transition that must be accompanied by a phonon) material. Materials that have a transition not accompanied by a large observeable change in their optical extinction spectrum are not available to be studied by the presented technique. In order to probe the nature of such transitions, one must turn to a technique that allows a more direct and less restrictive dynamic probe of the atomic structure. Recent developments in electron microscopy are showing that it is becoming more feasible to probe dynamic phenomena with both high spacial and time resolution in a relatively small laboratory setting.

The dynamic transmission electron microscopy (DTEM) experiments underway at Livermore National Labs show promising results [65-67]. They are able to initiate structural transformations using laser heating, and observe single shot images providing 20 nm spacial and 50 ns temporal resolution. These are lower limits are mainly imposed by space-charging effects and elecron-electron scattering, both of which arise from the large electron flux upon the sample. Complex analytical techniques and computer modeling could improve these figures in the near future.

Zewail and colleagues have used ultrafast electron diffraction to map molecular reactions [68-74]. This technique can yield a pair-distribution function for analytes with sub-picosecond resolution, and is shown to be useful in mapping reaction pathways that probe and identify intermediate molecules that are optically inactive. It utilizes a pump-probe technique in which the electron probe pulse is initiated by pumping the TEM filament with a short, NIR pulse that is similar to the kind utilized to initiate the shock pulses and produce super-continuum probe light here.

Structural studies on fast timescales, using x-rays as a probe have been producing interesting results for some time now [75-77], but emerging technologies will allow even greater experimental flexibility. At the Stanford linear accelerator, new experiments are coming online that will allow users of the facilities to probe samples using ~50 fs hard x-ray pulse, in order to generate femtosecond x-ray diffraction signals. This represents the next generation of x-ray beamline experiments. They will be able to do pump-probe x-ray diffraction with femtosecond resolution, results of which are forthcoming.

The above techniques all utilize optical pulses to pump the samples. The flexibility of the

techniques described to be able to probe optically “dark” analytes, opens a wide range of possibilities for future studies. Adapting these techniques to probe a sample undergoing shock-compression would provide a powerful tool for investigating dynamic, microscopic structure at high pressures and temperatures.

Bibliography

[1] Y. B. Zel'dovich and Y. P. Raiser, Physics of Shock Waves and High-Temperature Hydrodynamic Phenomena (Dover Publications, Inc., 31 East 2nd Street, Mineola, NY, 1966).

[2] G. Duvall and R. Graham, *Rev. Mod. Phys.* **91,** 9561 (2002).

[3] H. Kim, S. Hambir, and D. Dlott, J. Phys. Chem. B **104,** 4239 (2000).

[4] J.E. Patterson, D. Dlott, J. Phys. Chem. B, **109,** 504 (2005).

[5] D.D. Dlott, Acc. Chem. Res. **33**, 37 (2000).

[6] O. JONES and R. Graham, in Accurate Characterization of the High Pressure Environment, edited by E. C. Lloyd (U.S. National Bureau of Standards, U.S. Government Print Office, Washington, D.C., 1971).

[7] Coombes, C. J. *J. Phys.* **2,** 441 (1972).

[8] Buffat, P.; Borel, J.-P. *Phys. Rev. A,* **13,** 2287 (1976).

[9] Castro, T.; Reifenberger, R.; Choi, E.; Andres, R. P. *Phys. Rev. B: Condens. Matter.* **42,** 8548 (1990).

[10] Beck, R. D.; St. John, P.; Homer, M. L.; Whetten, R. L. *Science* **253,** 879 (1994).

[11] Martin, T. P.; Naher, U.; Schaber, H.; Zimmermann, U. *J. Chem Phys.* **100,** 2322 (1994).

[12] A. N. Goldstein, C. M. Echer, and A. P. Alivisatos, Science **256,** 1425 (1992).

[13] S. Tolbert and A. P. Alivisatos, *Science* **265,** 373 (1994).

[14] L.E. Brus, *J. Chem. Phys.*, **80,** 9 (1984).

[15] A. P. Alivisatos, J. Phys. Chem **100,** 13226 (1996).

[16] R. Hoffmann, *Solids and Surfaces* (Wiley, New York, 1988).

[17] H. Drickamer, *Int. Rev. Phys. Chem.* **2,** 171 (1982).

[18] B.S. Kim, M.A. Islam,, L.E. Brus, I.P. Herman, J. App. Phys. **89,** 8127 (2001).

[19] S.H. Tolbert, A.B. Herhold, C.S. Johnson, and A.P. Alivisatos, *Phys. Rev. Lett.* **73,** 3266 (1994).

[20] F. Wooten, *Optical Properties of Solids* (Academic Press, Missouri, 1972).

[21] C.F. Bohren, *Absorption and Scattering of Light by Small Particles,* (Wiley, New York, 1983).

[22] P.B. Johnson, R.W. Christy, *Phys. Rev. B.,* **6,** 4370 (1972).

[23] U. Kreibig, *Optical Properties of Metal Clusters* (Springer-Verlag, New York, 1995).

[24] N. E. Christensen and B. O. Seraphin, *Phys. Rev. B.* **4,** 3321 (1971).

[25] J.L. Coffer, J. Shapley, H.G. Drickamer, *J. Am. Chem. Soc.* **112,** (1990).

[26] G. Williams, *Trans. Faraday Soc.*, **60,** 1556 (1964).

[27] KT Gahagan, DS Moore, DJ Funk, RL Rabie, SJ Buelow, JW Nicholson, *Phys. Rev. Lett.* **85,** 3205 (2000).

[28] I. Lee, J. R. Hill, H. Suzuki, D. Dlott, B. Baer, and E. L. Chronister, *J. Chem. Phys.* **103,** 8313 (1995).

[29] L.A. Zepeda-Ruiz, B. Sadigh, J. Biener, A.M. Hodge, A.V. Hamza, *App. Phys. Lett.,* **91,** 101907 (2007).

[30] F. Ercolessi, M. Parrinello and E. Tosatti, Philos. Mag. A 58, 213 (1988).

[31] Y. Wang, S. Teitel, and C. Dellago, Nano Letters **5**, 2174 (2005).

[32] D. Frenkel, B. Smit, Understanding Molecular Simulation, 2nd edition, Academic Press (2001).
[33] D. Weeks, D. Chandler, and H. C. Andersen, J. Chem. Phys. **54**, 5237 (1971).
[34] H. A. Spetzler, M. D. Meyer, Rev. Sci. Instrum **45**, 911 (1974).
[35] M. Parrinello, A. Rahman, J. Appl. Phys. **52**, 7182 (1981).
[36] I. Lee, J. R. Hill, and D. Dlott, Journal of Applied Physics **75**, 4975 (1994).
[37] G. Decher, *Science*, **277,** 1232 (1997).
[38] J. Schmitt, G. Decher, *Adv. Mater*. **9,** 1 (1997).
[39] F. Lancon, J.Ye, D. CAliste, T Radetic, A.M. Minor, U. Dahmen, Nano Lett. **10**, 695 (2010).
[40] G.L. Hornyak, C.R. Martin, *Thin Solid Films*, **303** (1997).
[41] J. Christian, *The Theory of Transformation in Metals and Alloys* (Pergamon, London, 1965).
[42] M.H.R. Lankhorst, B.W.S.M.M. Ketelaars, and R.A.M. Wolters, Nature Mater. **4,** 347 (2005).
[43] S.H. Lee, Y. Jung, and R. Agarwal, Nature Nanotech. **2,** 626 (2007).
[44] A. Cavalleri, M. Rini, H.H.W. Chong, S. Fourmaux, T.E. Glover, P.A. Heimann, J.C. Kieffer, and R.W. Shoenlein, Phys. Rev. Lett. **95,** 067405 (2005).
[45] G. Duvall and R. Graham, Rev. Mod. Phys. **91,** 9561 (2002).
[46] I. Lee, J.R. Hill, H. Suzuki, D. Dlott, B. Baer, and E.L. Chronister, J. Chem. Phys. **103,** 8313 (1995).
[47] M. Knudson and Y. Gupta, J. Appl. Phys. **91,** 9561 (2002).
[48] K. Jacobs, D. Zaziski, E. Scher, A. Herhold, and A.P. Alivisatos, Science **293,** 1803 (2001).
[49] B. Morgan and P. Madden, Phys. Chem. Chem. Phys. **8,** 3304 (2006).
[50] M. Grunwald, E. Rabani, and C. Dellago, Phys. Rev. Lett. **96,** 255701 (2006).
[51] S. Tolbert and A.P. Alivisatos, J. Chem. Phys. **102,** 4642 (1995).
[52] C. Chen, A.B. Herhold, C. Johnson, and A.P. Alivisatos, Science **276,** 398 (1997).
[53] C.B. Murray, D.J. Norris, and M.G. Bawendi, J. Am. Chem. Soc. **115,** 8706 (1993).
[54] S.H. Tolbert, A.B. Herhold, C.S. Johnson, and A.P. Alivisatos, Phys. Rev. Lett. **73,** 3266 (1994).
[55] M. Grunwald and C. Dellago, Nano Lett. **9,** 2099 (2009).
[56] J.D. Kennedy and W.B. Benedick, J. Phys. Chem. Solids **27,** 125 (1966).
[57] D. Turnbull, J. Chem. Phys. **18,** 198 (1950).
[58] S. Kodiyalam, R.K. Kalia, H. Kikuchi, A. Nakano, F. Shimojo, and P. Vashishta, Phys. Rev. Lett. **86,** 55 (2001).
[59] Z. W. Shan, G. Adesso, A. Cabot, M. P. Sherburne, S. A. Syed Asif, O. L. Warren, D. C. Chrzan, A. M. Minor, and A. P. Alivisatos, Nature Materials **7,** 947 (2008).
[60] D. Zaziski, S. Prilliman, E. Scher, M. Casula, J. Wickham, S. M. Clark, and A. P. Alivisatos, Nano Letters **4,** 943 (2004).
[61] Y. D. Yin and et. al., Science **304,** 711 (2004).
[62] O. Friedl, C. Motz, H. Peterlik, S. Puchegger, N. Reger, and R. Pippan, Metallurgical and Materials Transactions B, **39B,** 135 (2008).
[63] D. E. Grady, International Journal of Engineering Science **22,** 1181 (1984).
[64] M. Armstrong, B. Reed, B. Torralva, N. Browning, Appl. Phys. Lett. **90,** 114101 (2007).

[65] M. Armstrong, K. Boyden, N. Browning, G. Campbell, J. Colvin, W. DeHope, A. Frank, D. Gibson, F. Hartemann, J. Kim, Ultramicroscopy, **107,** 347 (2007).
[66] T. Lagrange, M. Armstrong, K. Boyden, C. Brown, G. Campbell, J Colvin, W. DeHope, A. Frank, D. Gibson, F. Hartemann, Appl. Phys. Lett., **89,** 044105 (2009).
[67] A. Gahlmann, S. Park, A. Zewail, J. Am. Chem. Soc., **131,** 2806 (2008).
[68] Y. He, A. Gahlmann, J Feenstra, S Park, A Zewail, Chemistry-An Asian Journal, **1,** 56 (2006).
[69] H. Ihee, V. Lobastov, U. Gomez, B. Goodson, R Srinivasan, C. Ruan, A. Zewail, Science, **291,** 458 (2001).
[70] V. Lobastov, R. Srinivasan, B. Goodson, C. Ruan, J. Feenstra, A. Zewail, J. Phys. Chem. A, **105,** 1114 (2001).
[71] S. Park, J. Feenstra, A. Zewail, J. Chem. Phys.,**124,** 174707 (2006).
[72] R. Srinivasan, J. Feenstra, S. Park, S. Xu, Z. Zewail, Science, **307,** 558 (2005).
[73] R. Srinivasan, V. Lobastov, C. Ruan, A. Zewail, Helvetica chimica acta, **86,** 1761 (2003).
[74] D. Daranciang, H. Wen, M. Highland, B. Perkins, N. Brandt, K. Nelson, J. Larsson, D. Walko, E. Dufresne, P. Fuoss, G.B. Stephenson, and A.M. Lindenberg, *Ultrafast Phenomena XVII: Proceedings of the 17th International Conference* (2010).
[75] "Ultrafast x-ray scattering in solids", D.A. Reis and A.M. Lindenberg, in *Light Scattering in Solids IX*, Edited by M. Cardona and R. Merlin, (2007).
[76] A.M. Lindenberg, I. Kang, S.L. Johnson, R.W. Falcone, P.A. Heimann, Z. Chang, *Opt. Lett.* **27,** 869 (2002).
[77] J. Larsson, P.A. Heimann, A.M. Lindenberg, P.J. Schuck, P.H. Bucksbaum, R.W. Lee et al., *Appl. Phys. A,* **66,** 587 (1998).
[78] S. Hambir, H. Kim, D. Dlott, and R. Frey, Journal of Applied Physics **90**, 5139 (2001).